Photovoltaic solar cell technologies: analysing the state of the art

Pabitra K. Nayak[1], Suhas Mahesh[1], Henry J. Snaith[1] and David Cahen[2]*

Abstract | The remarkable development in photovoltaic (PV) technologies over the past 5 years calls for a renewed assessment of their performance and potential for future progress. Here, we analyse the progress in cells and modules based on single-crystalline GaAs, Si, GaInP and InP, multicrystalline Si as well as thin films of polycrystalline CdTe and $CuIn_xGa_{1-x}Se_2$. In addition, we analyse the PV developments of the more recently emerged lead halide perovskites together with notable improvements in sustainable chalcogenides, organic PVs and quantum dots technologies. In addition to power conversion efficiencies, we consider many of the factors that affect power output for each cell type and note improvements in control over the optoelectronic quality of PV-relevant materials and interfaces and the discovery of new material properties. By comparing PV cell parameters across technologies, we appraise how far each technology may progress in the near future. Although accurate or revolutionary developments cannot be predicted, cross-fertilization between technologies often occurs, making achievements in one cell type an indicator of evolutionary developments in others. This knowledge transfer is timely, as the development of metal halide perovskites is helping to unite previously disparate, technology-focused strands of PV research.

Sunlight is the most abundant, safe and clean energy source for sustainably powering economic growth. One of the most efficient and practical ways to harness sunlight as an energy source is to convert it into electricity using solar cells. However, there is an upper limit to the light-to-electrical power conversion efficiency (PCE, which is the ratio between the incident solar photon energy and the electrical energy output) of single-junction solar cells that is determined by the Shockley–Queisser (SQ) model and formalism[1]. Within the SQ formalism, it is postulated that all photons with energies above the bandgap (E_g) create free electrons and holes, which, with perfect charge-selective contacts, yields one electron per absorbed photon to contribute to the electrical current. The SQ model also stipulates that all electron–hole recombination events, which occur when the solar cell is generating power, are the inverse process to light absorption and therefore radiative, that is, they result in the re-emission of light. The SQ limit is based purely on thermodynamic considerations and takes the optical absorption edge, the solar spectrum and the operating temperature of the solar cell as the only inputs for the calculation of PCE. The efficiency of real-world single-junction solar cells will always be below the SQ limit, as real material properties come into play; for example, the absorption edge is not a step function, as assumed by the SQ model, and real materials have defects, which lead to non-radiative recombination (that is, the generation of heat instead of re-emission as light). However, by evaluating the present performance and understanding the fundamental limits associated with a particular cell type and technology, it is possible to assess how real-world cells deviate from their SQ limit and how they can be adapted to more closely approach this limit.

The notable progress in the development of photovoltaic (PV) technologies over the past 5 years necessitates the renewed assessment of state-of-the-art devices. Here, we present an analysis of the performance of 'champion' solar cells (that is, cells with the highest PCE values measured under the global AM 1.5 spectrum (1,000 W m^{-2})) for different types of PV technologies. We begin by defining the PV gap, which enables us to objectively compare different PV technologies. We then compare the progress, performance and losses associated with each PV technology. Finally, we provide an outlook on the possibilities for progress for different PV technologies on the basis of their current performance.

How well a semiconductor functions as a solar absorber material in a PV cell is governed primarily by the value of its bandgap. In our previous analyses of solar cell performance[2,3], we used the optical bandgap values of the absorbing material when a reliable value

[1]*Clarendon Laboratory, Department of Physics, University of Oxford, Oxford, UK.*

[2]*Department of Materials and Interfaces, Weizmann Institute of Science, Rehovot, Israel.*

**e-mail: pabitra.nayak@physics.ox.ac.uk*

https://doi.org/10.1038/s41578-019-0097-0

was available and, in other cases, the onset of the external quantum efficiency (EQE), which can be subjective, to compare the parameters of solar cells. Here, we adopt the distributed SQ gap method[4] to define the bandgap, which enables a consistent comparison between technologies. Moreover, we present the rationale behind the theoretical assessment of solar cell efficiencies, highlighting and quantifying the impact of both electronic disorder in the solar absorber material and electron–hole recombination (radiative versus non-radiative) on the efficiency of a cell. We derive a simple analytical relationship between the open-circuit voltage (V_{OC}) and a few properties of the solar absorber materials and solar cells, which make it possible to accurately estimate the V_{OC} or radiative efficiency of a cell without the need for complex calculations. When possible, we discuss the reasons behind the recent development in solar cell performance parameters and assess how far these parameters can be expected to further improve with the available technology and current state-of-the-art materials. We also focus on the interfaces within cells and their impact on solar cell performance and discuss how the evolution of interfacial materials has contributed to the development of solar cells.

One of the key results of our analysis is that in organic solar cells, PCE loss owing to electronic disorder and the sizeable binding energy of the excitons has been almost completely eliminated in the latest devices. The radiative efficiency is the main parameter that remains to be enhanced to make cells based on conjugated organic semiconductors competitive with the best technologies. On the downside, we infer that contemporary sustainable chalcogenide thin-film materials have such a high level of intrinsic static disorder that they will be incapable of yielding competitively efficient solar cells. Barring unforeseen developments to bypass the disorder issue, chalcogenide-based cells are likely to follow the fate of cells based on hydrogenated amorphous Si (often denoted as a-Si:H, but we use a-Si here), which have shown almost no progress over the past 10 years and have relatively low efficiencies, which can be traced back, at least in part, to their strong static disorder.

Arguably, the most remarkable progress over the past 5 years has been with halide-perovskite-based devices, for which the PCEs of laboratory cells now match those of the best established inorganic polycrystalline technologies. Although reported large-area perovskite cell and especially module performances, as well as cell stabilities, still lag behind those of established PV technologies, the rate of improvement in large-area cell performance and cell stability is promising. Taking cues from the development of other PV technologies, we extrapolate that the performance of halide perovskite cells and modules may soon reach that of the more mature polycrystalline technologies.

Defining the photovoltaic bandgap

Despite the fact that the bandgap is a fundamental material property, there remains considerable ambiguity over how to determine the bandgap and which methods for determining bandgaps are most relevant for PVs. Reliable optical bandgap values are often not available. Without reliable optical absorption data to extract bandgaps, we cannot make objective comparisons of cell parameters, including the V_{OC}, short-circuit current density (J_{SC}), voltage and current density at the maximum power point (V_{MP} and J_{MP}, respectively) and fill factor (FF) (Supplementary Fig. 1), of different cell types. There is increasing prominence of new types of cells, particularly metal halide perovskites (ABX_3, where A is an organic or inorganic cation, B is a metal cation and X is a halide); sustainable chalcogenides, such as $Cu_2ZnSnS_{4-y}Se_y$ (CZTSS) and Cu_2ZnSnS_4 (CZTS); and organic PVs (OPVs), which often lack reliable bandgap values or even a definition of a bandgap for the latter. Therefore, we use EQE data to determine a PV gap (E_g^{PV}), which is a weighted distribution of SQ bandgaps[4] (see Supplementary Fig. 2 and Supplementary Table 1 for the comparison of E_g^{PV} values with known optical bandgaps or lowest optical transition energies).

E_g^{PV} is given by

$$E_g^{PV} = \int_a^b E_g P(E_g) \mathrm{d}E_g \Big/ \int_a^b P(E_g) \mathrm{d}E_g \quad (1)$$

where $P(E_g) = \frac{\mathrm{d}}{\mathrm{d}E}\mathrm{EQE}(E)$ is the probability distribution function of the distribution of SQ-type bandgap energies and E is the photon energy. The maximum of $\frac{\mathrm{d}}{\mathrm{d}E}$ EQE gives an approximate E_g^{PV} value and can be used for all practical purposes if $P(E_g)$ is approximately Gaussian. To avoid noisy data, the integration limits are set to a and b, the photon energies for which $P(E_g)$ equals 50% of its maximum on either side of that maximum.

E_g^{PV} is called the PV gap to stress that its value need not be, and often will not be, the same as that determined from pure optical experiments, that is, the optical bandgap. As a simple illustration, as the thickness of a solar absorber material is increased, the E_g^{PV} of a cell comprising this absorber shifts to lower energies. By contrast, the optical bandgap, which is an intrinsic property of the material, will be unchanged.

The different methods to determine the relevant bandgaps for solar cells have previously been analysed[5]. For OPVs, it was suggested that the intersection point of the absorption and emission spectra of the lowest bandgap material can be used as an effective optical bandgap. However, for cells based on other absorber materials, it was suggested that E_g^{PV} should be used because it is determined from a physically meaningful extension of the SQ theory and in a mathematically consistent way that enables comparison of solar cell parameters between different types and architectures of PV cells[4].

Energy losses

Owing to thermodynamic factors (equation 2), at temperatures >0 K, it is not possible to convert all the energy associated with a separated electron–hole pair into usable free energy, even after thermalization of the carriers to the band edges. The V_{OC} of a solar cell in the SQ limit (V_{OC}^{SQ}) is given by equation 2 (REFS[6,7]) (see the Supplementary Information for the derivation of the analytical expression of qV_{OC}^{SQ}).

$$qV_{OC}^{SQ} = E_g^{PV}\left(1-\frac{T_A}{T_S}\right) + kT_A\ln\left(\frac{\gamma\left(E_g^{PV}, T_S\right)}{\gamma\left(E_g^{PV}, T_A\right)}\right) - kT_A\ln\left(\frac{\Omega_{out}}{\Omega_{in}}\right) \quad (2)$$

where $\gamma(E_g^{PV}, T) = T((E_g^{PV})^2 + 2kTE_g^{PV} + 2k^2T^2)$. Here, E_g^{PV} is equivalent to the SQ bandgap of the absorber in the solar cell; q is the elementary charge; T_A and T_S are the temperatures (in Kelvin) of the solar cell and the Sun, respectively; Ω_{out} and Ω_{in} are the solid angles for the emitted and absorbed photons, respectively; and k is the Boltzmann constant.

Attaining the radiative limit (the point at which, at open circuit, the photogenerated carriers can escape the system only as emitted photons) does not require a step-function absorptance. Correspondingly, the V_{OC} of the cell in the radiative limit (V_{OC}^{Rad}) is different from V_{OC}^{SQ} if the absorptance of the cell deviates from a step function (see the Supplementary Information for the relationship between qV_{OC}^{SQ} and qV_{OC}^{Rad}). The less steep the rise in EQE, the larger the dark recombination current density and the lower V_{OC}^{Rad} is with respect to V_{OC}^{SQ}. We refer to the difference in these two V_{OC} values as the radiative recombination loss.

Owing to the occurrence of non-radiative recombination in any real PV system, as well as the subunity efficiency of photon out-coupling, the experimentally observed V_{OC} values of solar cells are lower than the radiative limit and are given by[8,9]

$$qV_{OC}^{cell} = qV_{OC}^{Rad} - kT_A\left|\ln(\eta_{ext})\right| \quad (3)$$

where η_{ext} is the EQE for electroluminescence of the solar cell.

At open circuit, the net rate of flow of the charge carriers from the cell is zero (resulting in zero power output), and thus, the difference between the (quasi-) electrochemical potentials of the electrons and holes is at its highest. Between open circuit and short circuit, there is a voltage–current combination that yields the maximum power. At maximum power, the non-zero rate of flow of charge carriers from the cell lowers the steady-state concentrations of the carriers inside the cell, which affects the (quasi-)electrochemical potentials of the charge carriers such that V_{MP} is related to V_{OC} and is always less than V_{OC} (see the Supplementary Information for the relationship between V_{MP} and V_{OC}). The operational loss (OL) in energy in a solar cell is thus given by $E_g^{PV} - qV_{MP}$. The total operational loss can be written as the sum of the contributing loss mechanisms:

$$\begin{aligned} \text{OL} = {} & \text{SQ loss} \\ & + \text{deviation from the EQE in the SQ limit} \\ & + \text{non-radiative recombination loss} \\ & + \text{loss due to operation at maximun} \\ & \text{power and contact resistance} \end{aligned} \quad (4)$$

Mathematically, the operational loss can be expressed as (see the Supplementary Information for the derivation of equation 5)

$$\begin{aligned} \text{OL} = {} & \left(E_g^{PV}\frac{T_A}{T_S}\right) - kT_A\ln\left(\frac{\gamma\left(E_g^{PV}, T_S\right)}{\gamma\left(E_g^{PV}, T_A\right)}\right) \\ & + kT_A\ln\left(\frac{\Omega_{out}}{\Omega_{in}}\right) + kT_A\ln\left(\frac{J_{SC}^{SQ}}{J_{SC}}\right) \\ & + kT_A\ln\left(\frac{J_0^{Rad}}{J_0^{SQ}}\right) + kT_A\ln\left|(P_{esc})\right| \\ & + kT_A\ln\left|\left(\frac{\eta_{int}}{1-\left(\eta_{int}\cdot P_{reabs}\right)}\right)\right| \\ & + nkT_A\ln\left(\frac{qV_{OC}^{cell}}{nkT_A} - \ln\left(\frac{qV_{OC}^{cell}}{nkT_A}+1\right)+1\right) \\ & + \text{loss due to the contact resistance} \end{aligned} \quad (5)$$

Here, J_{SC}^{SQ} and J_0^{SQ} are the short-circuit photocurrent density and dark saturation current density in the SQ limit, respectively, and J_0^{Rad} is the dark saturation current density in the radiative limit. η_{int} is the internal luminescence efficiency, and P_{esc} and P_{reabs} are the probabilities that a photon escapes or is reabsorbed by the cell, respectively. The components that contribute to the operational loss are shown in FIG. 1a. On the right-hand side of equation 5, the first three terms correspond to the net loss ($E_g^{PV} - qV_{OC}^{SQ}$) at open circuit in the SQ limit, which is unavoidable in any single-junction cell. The net loss at open circuit shows a quasi-linear relationship with E_g^{PV} (Supplementary Fig. 4) for E_g^{PV} values in the range 1.0–2.5 eV, which spans almost all bandgaps of interest for solar cells. This quasi-linear relationship enables us to provide the following simplified analytical expression to calculate the V_{OC}^{SQ} of a cell operating at room temperature (298 K).

$$qV_{OC}^{SQ} = 0.941E_g^{PV} - 0.171\ \text{eV} \quad (6)$$

The slope of the plot of qV_{OC}^{SQ} versus E_g^{PV} (FIG. 1b) is dominated by the first term of equation 2, and the value of $(1 - T_A/T_S)$ at 298 K is 0.95. As the other terms that are dependent on E_g^{PV} are in the arguments of logarithms in the second term of equation 2, they have minimal influence on the slope, resulting in a slight reduction only. The intercept of the plot of qV_{OC}^{SQ} versus E_g^{PV} is mainly determined by the part of the second term that is independent of E_g^{PV} and the third term of equation 2. The V_{OC} of the certified champion cells are shown in FIG. 1b (see TABLE 1 for the E_g^{PV} and V_{OC} values of certified champion cells and Supplementary Table 2 for the PCE, area and FF values of these cells).

The fourth and fifth terms on the right-hand side of equation 5 correspond to the extra radiative recombination loss due to the non-step-function absorptance in the cell, which depends mainly on the static electronic disorder in the absorber. The electronic disorder, which can be quantified by the steepness of the absorption onset, and the exponential gradient of the absorption tail, termed the Urbach energy (E_U), are discussed further below. High-quality semiconductor materials typically have E_U values in the range 7–15 meV, which

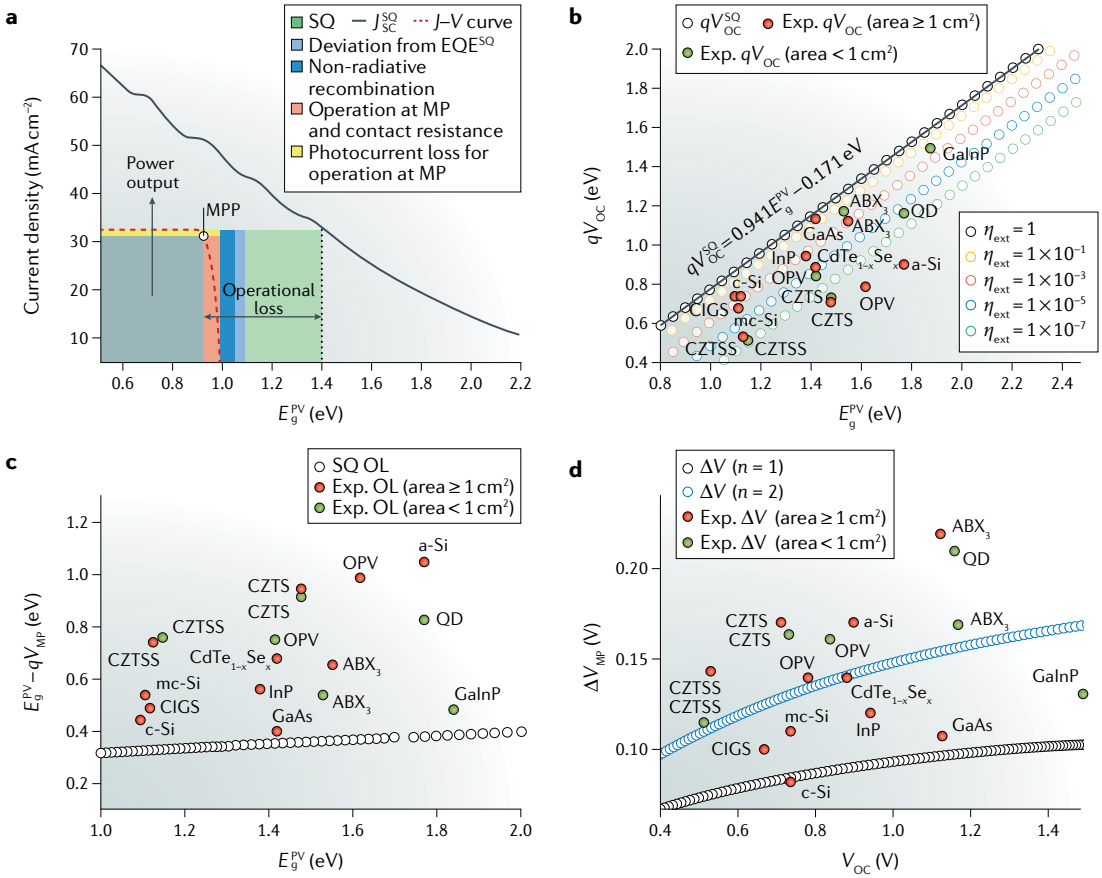

Fig. 1 | **Operational losses in solar cells. a** | Components of the operational loss (OL) in solar cells (inspired by the analysis of Ekins-Daukes and Hirst[70]). The maximum short-circuit photocurrent density in the Shockley–Queisser (SQ) limit (J_{SC}^{SQ}) is plotted as a function of the photovoltaic gap (E_g^{PV}). The dotted vertical line indicates the E_g^{PV} of the cell, and the red dashed line indicates the current density–voltage (*J*–*V*) curve of the cell. The grey area represents the power output of the cell (where MPP is the maximum power point). The losses include those associated with operation at maximum power (MP) and the deviation from the external quantum efficiency in the SQ limit (EQE^{SQ}). **b** | Comparison of the experimental open-circuit voltage (V_{OC}) of different solar cell technologies and the theoretical values of the V_{OC} in the SQ limit (V_{OC}^{SQ}) versus E_g^{PV}. The relationship between qV_{OC}^{SQ} (where *q* is the elementary charge) and E_g^{PV} is quasi-linear for typical solar cells with $E_g^{PV} = 1$–2.5 eV. The values of qV_{OC}^{SQ} (open circles) are calculated for different values of the external quantum efficiency for electroluminescence (η_{ext}) of the cell with $qV_{OC}^{SQ} = qV_{OC}^{Rad}$ (where V_{OC}^{Rad} is the V_{OC} in the radiative limit). The experimental values include those for small-area cells (<1 cm^2) and cells with areas of ≥1 cm^2. **c** | Experimental OLs at maximum power versus E_g^{PV} for cells with areas of <1 cm^2 and ≥1 cm^2. For comparison, the theoretical maximum OLs (open black circles) have been calculated from thermodynamic considerations in the SQ limit. **d** | Comparison of the experimental and theoretical voltage losses ($\Delta V = V_{OC} - V_{MP}$, where V_{MP} is the voltage at maximum power) for operation at maximum power. The expected ΔV for a given V_{OC} has been calculated for ideal contacts and only radiative recombination with a diode ideality factor (*n*) of 1 and for ideal contacts with $n = 2$. The experimental values of ΔV have been determined for both small-area (<1 cm^2) and larger-area (≥1 cm^2) cells. ABX$_3$, metal halide perovskite (where A is an organic or inorganic cation, B is a metal cation and X is a halide); a-Si, amorphous Si; CIGS, CuIn$_x$Ga$_{1-x}$Se$_2$; c-Si, single-crystalline Si; CZTS, Cu_2ZnSnS_4; CZTSS, $Cu_2ZnSnS_{4-y}Se_y$; mc-Si, multicrystalline Si; OPV, organic photovoltaic; QD, quantum dot. Panel **c** is adapted with permission from REF.[3], Wiley-VCH.

results in an extra loss of ~10 meV in the V_{OC} in the radiative limit. The sixth and seventh terms of equation 5 together ($kT_A|\ln(\eta_{ext})|$) correspond to the loss due to the non-radiative recombination and inefficiency in photon out-coupling. These two terms depend on the electronic quality (that is, density of non-radiative recombination centres) of the absorber and interfacial material and on the device architecture. FIGURE 1b shows the expected qV_{OC} for different values of η_{ext} when $qV_{OC}^{SQ} = qV_{OC}^{Rad}$.

We can modify equation 6 (at 298 K) to be an accurate predictor of V_{OC} as a function of E_g^{PV} and η_{ext} for a solar cell with a relatively steep absorption onset

$$qV_{OC} = 0.941E_g^{PV} - \left(0.181 + 0.0257|\ln(\eta_{ext})|\right) \text{ eV} \quad (7)$$

The above analytical expression can be used to gauge the η_{ext} of a cell from its V_{OC} and E_g^{PV} values. To check the applicability of equation 7, we compared the values of η_{ext} calculated from qV_{OC} and E_g^{PV} with the experimentally determined η_{ext} values for different types of single-crystalline GaInP and metal halide perovskite cells, as well as single-crystalline Si (c-Si), CuIn$_x$Ga$_{1-x}$Se$_2$ (CIGS) and single-crystalline GaAs cells (Supplementary Fig. 5 And Supplementary Table 3). We find good agreement between the calculated and measured values of η_{ext}.

Table 1 | **Photovoltaic gaps and voltage efficiencies of champion laboratory cells**

Cell type	$E_{g_d}^{PV}$ (eV)[a] ($(\frac{d}{dE}EQE)_{Max}$ (eV))	V_{OC} (V)	V_{MP} (V)	$E_g^{PV} - qV_{OC}$ (eV)	OL (eV)	qV_{OC}/E_g^{PV} (%)	qV_{MP}/E_g^{PV} (%)	qV_{MP}^{SQ}/E_g^{PV} (%)	Loss from contacts (mV)[b]	Refs[c]
Single-crystalline materials										
c-Si	1.10 (1.07)	0.74	0.66	0.36	0.44	67	60	71	1	74
GaAs	1.42 (1.41)	1.13	1.02	0.29	0.40	80	72	75	14	10
InP	1.38 (1.34)	0.94	0.82	0.44	0.56	68	59	75	30	74
GaInP[d]	1.88 (1.84)	1.49	1.36	0.39	0.52	79	72	79	28	72
Polycrystalline materials										
mc-Si	1.11 (1.09)	0.67	0.57	0.44	0.54	60	51	71	20	81
$CdTe_{1-x}Se_x$	1.42 (1.42)	0.88	0.74	0.54	0.68	62	52	75	52	82
CIGS	1.12 (1.12)	0.74	0.63	0.38	0.49	66	56	71	27	20
CZTSS	1.13 (1.14)	0.53	0.39	0.60	0.74	47	34	72	68	10
CZTS	1.48 (1.46)	0.71	0.54	0.77	0.94	48	36	76	88	74
ABX_3	1.55 (1.55)	1.12	0.90	0.43	0.65	72	58	77	125	81
Other materials										
a-Si	1.77 (1.71)	0.90	0.73	0.87	1.04	51	41	78	81	82
OPV (Toshiba)	1.62 (1.63)	0.78	0.64	0.84	0.98	48	41	77	55	82
QD[d]	1.77 (1.78)	1.16	0.95	0.61	0.82	65	54	78	114	54

The photovoltaic gap (E_g^{PV}) is determined from the external quantum efficiency (EQE) of the cell. ABX_3, metal halide perovskite; a-Si, amorphous Si; CIGS, $CuIn_xGa_{1-x}Se_2$; c-Si, single-crystalline Si; CZTS, Cu_2ZnSnS_4; CZTSS, $Cu_2ZnSnS_{4-y}Se_y$; mc-Si, multicrystalline Si; OL, operational loss ($E_g^{PV} - qV_{MP}$); OPV, organic photovoltaic; q, elementary charge; QD, quantum dot; V_{MP}, experimentally determined voltage at maximum power; V_{MP}^{SQ}, voltage at maximum power in the Shockley–Queisser limit; V_{OC}, open-circuit voltage. [a]The E_g^{PV} values deviate slightly for some materials from the maximum of $\frac{d}{dE}EQE$, which is denoted as $(\frac{d}{dE}EQE)_{Max}$ and is given in parentheses. [b]Includes loss due to non-ideal (that is, with a diode ideality factor of >1) recombination. [c]References for the EQE values used for the calculation of E_g^{PV} and current–voltage curves for solar cell parameters. [d]Area <1 cm^2.

The eighth term in equation 5 represents the loss due to operation at maximum power. FIGURE 1c compares the experimental operational loss ($E_g^{PV} - qV_{MP}$) at maximum power with the loss in the SQ limit ($E_g^{PV} - qV_{MP}^{SQ}$), which is unavoidable for systems that fit the SQ model. In real cells, there is also an additional loss due to the non-zero series resistance of the charge-collecting contacts. This practical loss is given by the difference between ($V_{OC}^{cell} - V_{MP}$) and $(nkT_A/q)\ln[qV_{OC}^{cell}/nkT_A - \ln(qV_{OC}^{cell}/nkT_A + 1) + 1]$ (TABLE 1) and is dominated by the contributions from the contacts that are an integral part of a solar cell.

The expected voltage loss versus the V_{OC} of a cell and the experimentally observed voltage loss are shown in FIG. 1d. The comparison illustrates that the voltage loss, beyond V_{OC}, varies greatly between the different cell technologies. For example, even though cells based on CIGS, CZTS and c-Si have similar V_{OC} values, the calculated voltage losses beyond V_{OC} differ. The same is true for the InP, polycrystalline $CdTe_{1-x}Se_{1-x}$ and a-Si group of cells and for the ABX_3 metal halide perovskite and GaAs cells.

Photocurrent efficiency

A plot of the maximum J_{SC}^{SQ} versus E_g^{PV} is shown in FIG. 2a. The experimental photocurrents at short circuit and at maximum power for various cell types are also shown, providing a visual overview of the current efficiencies of the cells. The ratio J_{SC}/J_{SC}^{SQ} reflects the efficiency of photon capture and subsequent photocarrier generation and collection at the contacts of a cell; the values of J_{SC}/J_{SC}^{SQ} for the different cells are listed in TABLE 2. For cell operation at maximum power, some photogenerated carriers recombine and therefore do not contribute to the photocurrent; thus, J_{MP} is always less than J_{SC}. Equation 8 describes the relationship between J_{MP}, J_{SC} and V_{OC} (see the section 'Relationship between J_{MP}/J_{SC} and V_{OC}' in the Supplementary Information for the derivation).

$$\frac{J_{MP}}{J_{SC}} = \frac{V_{OC}' - \ln(V_{OC}' + 1)}{V_{OC}' - \ln(V_{OC}' + 1) + 1} \quad (8)$$

where $V_{OC}' = \frac{qV_{OC}^{cell}}{nkT_A}$

The J_{MP}/J_{SC} values calculated using equation 8 for two different values of the diode ideality factor (n) and the experimentally determined J_{MP}/J_{SC} values (TABLE 2) are plotted against the V_{OC} in FIG. 2b. The observed deviation of the experimental values from the ideal values (that is, for $n = 1$) indicates the loss of photogenerated carriers, which leads to a decrease in the cell efficiencies. The additional loss of photocurrent beyond what is required to maintain the V_{MP} of a cell indicates the presence of more than one carrier recombination pathway in the system. Non-radiative carrier recombination, in the bulk and at the interfaces, together with the presence of shunt resistances contribute to the loss in

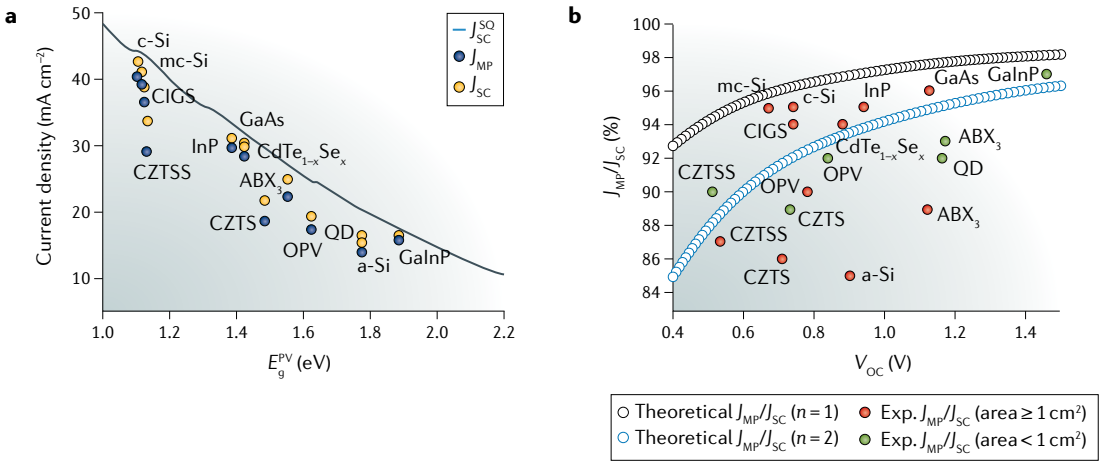

Fig. 2 | **Photocurrent efficiency in solar cells. a** | Maximum possible short-circuit photocurrent density in the Shockley–Queisser limit (J_{SC}^{SQ}) versus the photovoltaic gap (E_g^{PV}) compared with the experimental photocurrent density at short circuit (J_{SC}) and maximum power (J_{MP}) for the champion cells at AM 1.5 G illumination (ASTM G-173-03 global, see Reference https://rredc.nrel.gov/solar//spectra/am1.5/#about). **b** | Theoretical J_{MP}/J_{SC} values versus the open-circuit voltage (V_{OC}) (from equation 8) with a diode ideality factor (n) of 1 and 2. Experimental J_{MP}/J_{SC} values are for cells with areas of ≥1 cm^2 and <1 cm^2. ABX_3, metal halide perovskite (where A is an organic or inorganic cation, B is a metal cation and X is a halide); a-Si, amorphous Si; CIGS, $CuIn_xGa_{1-x}Se_2$; c-Si, single-crystalline Si; CZTS, Cu_2ZnSnS_4; CZTSS, $Cu_2ZnSnS_{4-y}Se_y$; mc-Si, multicrystalline Si; OPV, organic photovoltaic; QD, quantum dot. Panel **a** is adapted with permission from REF.[3], Wiley-VCH.

photogenerated carriers. Not surprisingly, we find that the single-crystalline-based device technologies, that is, c-Si, InP, GaAs and GaInP, show the highest J_{MP}/J_{SC} values, whereas those based on two polycrystalline materials, namely, CZTSS and CZTS, and on a-Si show the poorest J_{MP}/J_{SC} values.

In the following, we discuss the observed photocurrent efficiencies along with the progress, performance and losses associated with each PV technology.

Progress and performance of solar cells

Single-crystalline cells

Single-crystalline GaAs. A solar cell based on single-crystalline GaAs has shown the highest PCE (29.1%) of any single-junction cell[10]. This high PCE is predominantly attributable to a remarkable value of V_{OC}. For high-performance cells, single-crystalline GaAs thin films made by epitaxial lift-off are used. This lift-off process enables the use of highly reflective back contacts instead of substrates that introduce parasitic absorbance. The near-unity photoluminescence quantum yield (PLQY) of the absorber material (~99.7%[11]), suppression of non-radiative recombination at the charge-collecting interfaces and the highly reflective back contact help the photons to be recycled before they escape the cell from the front surface (FIG. 3a–c). All these factors translate into the cell having a near-unity value of η_{ext} or external radiative efficiency[12]. Because GaAs has a very sharp absorption onset, $J_0^{SQ} \approx J_0^{Rad}$, and with η_{ext} approaching unity, the V_{OC} closely approaches the SQ limit[13] (FIG. 1b). The loss in photocurrent at short circuit (J_{SC}/J_{SC}^{SQ} = 93%; TABLE 2) could be partly due to shadowing from the top contact of the cell, which could be avoided if an all-back contact configuration could be realized. The value of J_{MP}/J_{SC} is close to optimal for the V_{OC} of the cell, but there is still scope for a 1% improvement.

Single-crystalline GaInP. Like GaAs, progress in single-crystalline GaInP technology can mostly be attributed to the development of new cell architectures[14]. GaInP (typically $Ga_{0.5}In_{0.5}P$) cells with an absorbing GaAs substrate in an upright configuration (Supplementary Fig. 6a) (for which P_{esc} = 0.015 and P_{reabs} = 0.60) can yield η_{ext} values of 0.04 for η_{int} = 1. By contrast, an inverted GaInP solar cell[14] (Supplementary Fig. 6a) with a good Au back reflector (with P_{esc} = 0.024 and P_{reabs} = 0.90) can reach an η_{ext} value of 0.25 for η_{int} = 1. The adoption of the inverted structure with a Au back reflector pushed the cell PCE to 20.8% by increasing V_{MP} and V_{OC} (REF.[14]). An additional increase in the PCE to 21.4% was achieved by tuning the stoichiometry (that is, the Ga:In ratio) of GaInP to achieve a slightly higher bandgap (Supplementary Fig. 6b), which further increased the V_{OC} of the cell. Note that the bandgap of GaInP can be tuned by stoichiometry and/or by the degree of structural ordering[15]. The photocurrent efficiency of this cell also increased owing to improved collection of carriers generated from the higher-energy photons, presumably owing to the improved electronic quality of GaInP. The high J_{MP}/J_{SC} and low operational loss for a 0.25 cm^2 cell[16] show that this technology is getting closer to the efficiencies (relative to the bandgap) that can be obtained with GaAs.

Single-crystalline InP. The champion cell based on single-crystalline InP now has a PCE of 24.2%, a significant improvement from the previous 22.1%. The new champion cell has both a higher J_{SC} and a higher V_{OC} than those of its predecessor. The increase in photocurrent efficiency is due to the high–low doping

Table 2 | **Photocurrent efficiency of champion laboratory cells**

Cell type	E_g^{PV} (eV)	J_{SC}^{SQ} (mA cm^{-2})	J_{SC} (mA cm^{-2})	J_{MP} (mA cm^{-2})	J_{SC}/J_{SC}^{SQ} (%)	J_{MP}/J_{SC}^{SQ} (%)	J_{MP}/J_{SC} (%)	Refs[a]
Single-crystalline materials								
c-Si	1.10	44.2	42.6	40.3	96	91	95	74
GaAs	1.42	32.0	29.8	28.5	93	89	96	10
InP	1.38	33.7	31.1	29.6	92	88	95	74
GaInP[b]	1.88	17.4	16.3	15.8	94	91	97	72
Polycrystalline materials								
mc-Si	1.11	44.1	41.1	39.1	93	89	95	81
$CdTe_{1-x}Se_x$	1.42	32.0	30.2	28.3	94	88	94	82
CIGS	1.12	43.8	38.8	36.4	89	83	94	20
CZTSS	1.13	43.4	33.6	29.1	77	67	87	10
CZTS	1.48	29.6	21.8	18.7	74	63	86	74
ABX_3	1.55	27.3	24.9	22.2	91	84	89	81
Other materials								
a-Si	1.77	20.4	16.4	13.9	80	68	85	82
OPV (Toshiba)	1.62	24.8	19.3	17.3	78	70	90	82
QD[b]	1.77	20.3	15.2	14	75	69	92	54

The short-current density in the Shockley–Queisser limit (J_{SC}^{SQ}) is calculated from the global AM1.5 spectrum (ASTM G-173-03 global). Values of the maximum of $\frac{d}{dE}$EQE (where EQE is the external quantum efficiency) are given in TABLE 1. ABX_3, metal halide perovskite; a-Si, amorphous Si; CIGS, $CuIn_xGa_{1-x}Se_2$; c-Si, single-crystalline Si; CZTS, Cu_2ZnSnS_4; CZTSS, $Cu_2ZnSnS_{4-y}Se_y$; J_{MP}, current density at maximum power; mc-Si, multicrystalline Si; OPV, organic photovoltaic; QD, quantum dot. [a]References for the EQE values used for the calculation of the photovoltaic gap (E_g^{PV}) and current–voltage curves for solar cell parameters. [b]Area < 1 cm^2.

scheme (FIG. 3d) used in the emitter layer (which is the most heavily doped layer, the role of which is to inject and/or emit the carrier into a less doped base layer). The improvement in the V_{OC} is due to the lattice-matched (Al,In)As back-surface confinement layer (FIG. 3d). This layer provides an efficient barrier for the minority charge carrier, enabling charge recombination to take place in the low-doped InP base layer, which is mainly radiative in nature[17]. Despite the improvements, the operational loss and photocurrent efficiency (FIGS 1c,2a) in this technology are still far from their theoretical limits. With materials properties that are similar to those of GaAs and GaInP, and with E_g^{PV} = 1.38 eV, we expect the efficiency of this technology to edge closer to that of GaAs in the coming years, provided that the problems of interfacial recombination and parasitic absorbance can be overcome.

Single-crystalline Si. For almost 14 years, the highest PCE of a c-Si solar cell stood at 25%[18]. This c-Si solar cell had an area of 4 cm^2 and was based on the so-called passivated emitter and rear locally diffused (PERL) solar cell technology (FIG. 4a). However, this cell suffered from photocurrent losses due to shadowing from the front grid and non-radiative surface recombination due to the contacts. The interdigitated back contact (IBC) architecture (FIG. 4b) has two main advantages over the PERL cell with front and back contacts: first, without a top grid, light trapping and passivation on the top surface can be expanded without a shadowing effect, and second, the electrodes at the back can be placed close to each other to lower the series resistance, which decreases the operational loss.

To minimize non-radiative recombination at the surfaces as a result of the contacts, a Si heterojunction (SHJ) architecture (FIG. 4c) has been adopted. Within the SHJ architecture, a thin film of intrinsic hydrogenated amorphous Si (i:a-Si) is introduced between the absorber (c-Si) and either an n-doped or a p-doped a-Si layer to decouple passivation from charge collection (see Passivation of c-Si with a-Si section in the Supplementary Information).

The present champion c-Si cell has a PCE of 26.7% (with an area of 79 cm^2) and has a device structure (FIG. 4d) that blends concepts from the SHJ and IBC cells. Advances in processing technologies and continuing materials development for the microelectronics industry in order to obtain high-grade electronic quality Si crystals have made it possible to realize the present champion c-Si cell.

The question now is whether new technological advances can further increase the efficiency of c-Si technology. In our opinion, there is still room for improvement, particularly in the current efficiency. The photocurrent efficiency of the champion c-Si cell is lower than the SQ limit (J_{SC}/J_{SC}^{SQ} = 96%, TABLE 2) and comparable to that of the PERL cell despite having no front electrodes. An unavoidable loss in photocurrent (1–2%) is caused by the filtering effect from the a-Si layer, which is essential for the creation of the heterojunction. This loss manifests itself as a drop in the EQE at wavelengths of <500 nm (REFS[19,20]) (Supplementary Fig. 7). The gaps between the rear electrodes also contribute to the photocurrent loss, because light can pass through them rather than be reflected back into the

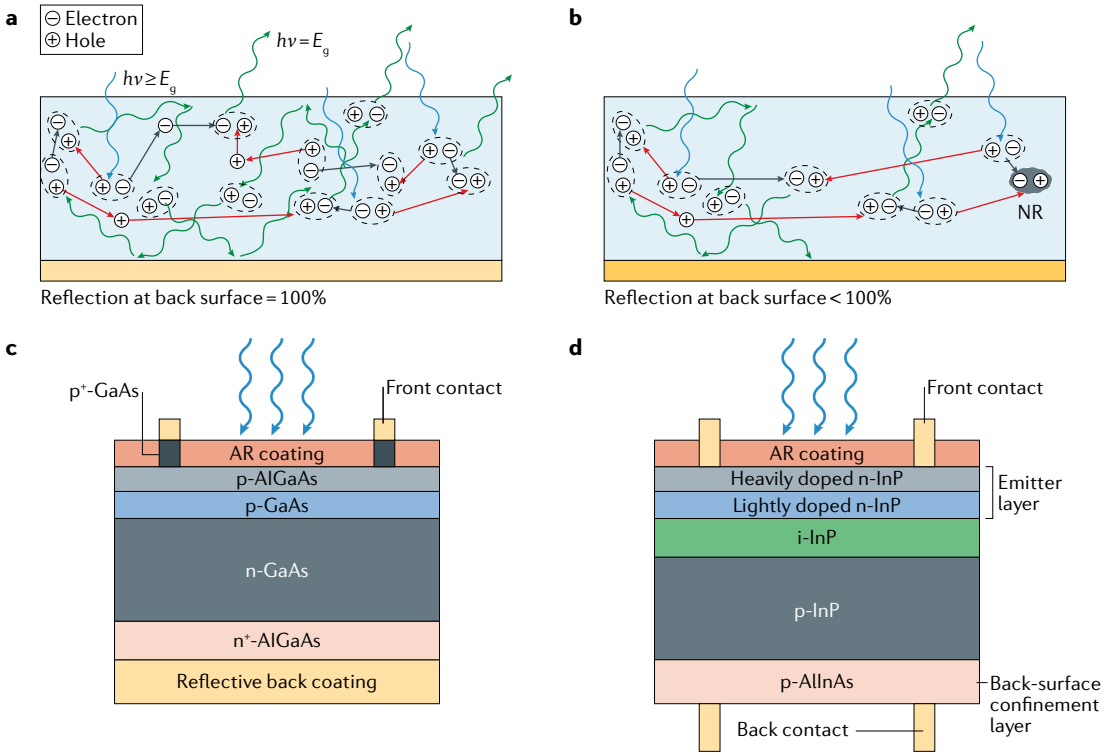

Fig. 3 | **Photon management and device architecture of GaAs and InP cells. a**,**b** | Panel **a** shows photon and charge-carrier management in a cell with an internal luminescence efficiency of 1 and a back surface that reflects 100% of photons. Panel **b** shows the photon and charge-carrier behaviour in a cell with non-radiative recombination (NR) and parasitic absorbance at the back surface. The blue and green arrows represent the incoming photons and the photons generated owing to the recombination of charge carriers, respectively. The black and red arrows show the propagation of the electrons and holes, respectively. **c** | Device architecture of a single-crystalline GaAs cell that comprises both n-type and p-type GaAs (n-GaAs and p-GaAs, respectively) as well as heavily doped n-type AlGaAs (n^+-AlGaAs), p-type AlGaAs (p-AlGaAs) and heavily doped p-type GaAs (p^+-GaAs). **d** | Device architecture of a single-crystalline InP cell that contains intrinsic, n-type and p-type InP (i-InP, n-InP and p-InP, respectively) as well as p-type AlInAs (p-AlInAs). *v*, photon energy; AR, anti-reflective; E_g, bandgap; *h*, Planck's constant.

Si layers. This problem can be mitigated by using reflective dielectric materials in the gaps. In sandwich-structured SHJ cells (FIG. 4c), in which the p and n contacts are on either side of the Si wafer, a V_{OC} of 750 mV has already been demonstrated[21]. Hence, a further increase in the V_{OC} of ~10 mV is expected[22] with the present SHJ–IBC architecture.

Increasing the V_{OC} of c-Si cells towards the SQ limit is very difficult owing to the limited photoluminescence efficiencies of even high-quality Si wafers. The highest-quality flat-zone c-Si material with a passivated surface has an experimentally determined η_{int} of only ~20%[23]. Commercially produced Si wafers have η_{int} values that are an order of magnitude lower[23]. The relatively low η_{int} values of commercial Si wafers are due to the indirect bandgap of Si, which is an intrinsic material property that cannot be altered for this form of Si. The indirect bandgap results in a lower absorbance coefficient, meaning that more material is needed to absorb all the sunlight. The large volume of the material, compared with other PV absorber materials, and the long carrier lifetimes mean that even low defect densities cause significant non-radiative recombination. The maximum possible PCE in c-Si is 29.4%, which takes into account the SQ limit and intrinsic materials properties of Si, especially Auger recombination[22].

Polycrystalline cells

Multicrystalline Si. Unlike c-Si, polycrystalline Si (known as multicrystalline Si (mc-Si)) has inherent grain boundaries and dislocations, which result in lower V_{OC} and V_{MP} values than those of c-Si cells (TABLE 1). Improvement in mc-Si technology over the past few years is due to the development of 'high-performance mc-Si', which has fewer structural defects[24]. n-Type high-performance mc-Si wafers benefit from the higher minority-carrier lifetime in n-type (holes) than in p-type (electrons) Si, which is due to the fact that Fe, one of the most important residual impurities in Si, is an effective electron scattering agent[25]. The champion mc-Si cell uses a diffused boron front emitter and full-area tunnelling oxide passivating rear contacts[26]. The photocurrent efficiency of this champion mc-Si cell is comparable to that of c-Si cells and superior to that of technologies based on other polycrystalline materials. However, as expected, the operational loss is higher than that of single-crystal-based technologies.

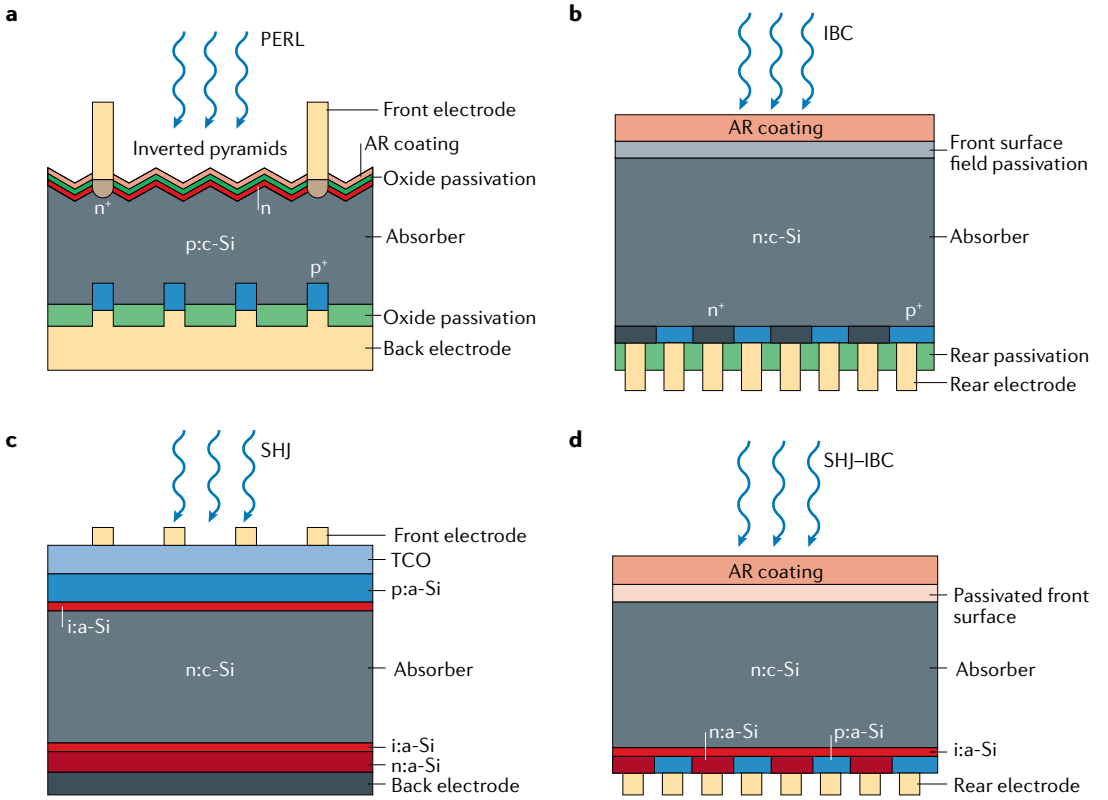

Fig. 4 | **Device architectures of different types of champion single-crystalline Si cells. a** | A passivated emitter and rear locally diffused (PERL) cell with both front and back contacts and with p-type single-crystalline Si (p:c-Si) as the absorber. This cell has achieved a record power conversion efficiency (PCE) of 25%[71]. **b** | An interdigitated back contact (IBC) homojunction solar cell with interdigitated heavily doped p (p^+)-diffused and n (n^+)-diffused regions in the Si substrate (n-type c-Si (n:c-Si)). The p^+ and n^+ regions are directly connected to the hole and electron contacts, respectively. The top surface of the Si absorber is passivated by the formation of a front surface (electric) field. The record PCE for this IBC cell is 25.2%[72]. **c** | Silicon heterojunction (SHJ) cell with top and bottom contacts and a thin film of intrinsic amorphous Si (i:a-Si). The p^+ and n^+ heterojunctions are created near the front and back surfaces, respectively. The transparent conducting oxide (TCO) layer acts as an electrode and as an anti-reflective (AR) coating. The record PCE of this cell is 25.1%[73]. **d** | A SHJ–IBC cell, which is a hybrid of device concepts from the SHJ and IBC cells, with interdigitated p^+ and n^+ heterojunction layers contacted by hole-collecting and electron-collecting electrodes, respectively. The SHJ–IBC cell has reached a record PCE of 26.7%[19,74]. The front of the n:c-Si wafer surface is textured (not shown in the figure) to minimize reflection and is passivated with a-Si. n:a-Si, n-type amorphous Si; p:a-Si, p-type amorphous Si.

CIGS. Upon comparing the EQE of champion CIGS ($CuIn_xGa_{1-x}Se_2$) cells from the past few years (FIG. 5a), we find a noticeable difference in the EQEs as the cell efficiency increases. The EQE of the cell with a PCE of 19.8% drops sharply for photon wavelengths of <520 nm. This decrease is a result of the combined effect of the inadequate diffusion length of the carriers and filtering from the CdS layer that is often used in these polycrystalline solar cells (see Supplementary Fig. 8a for a schematic of the device architecture of a CIGS cell). CdS, which is now often replaced by ZnS, is needed for both surface and interface passivation, which increases the V_{OC} but at the expense of the J_{SC}.

A major improvement in CIGS technology was a change in alkali metal ion treatment (from Na to K) after deposition of the CIGS layer. K^+ treatment modifies the chemical composition near the surface of the CIGS film by depleting Cu and Ga and introducing a substantial density of K^+ (REF.[27]). This change in composition enables shorter chemical bath CdS deposition times (yielding thinner CdS layers) to achieve the necessary surface passivation and inversion of the majority carrier type. Thinner CdS layers enable more photons with wavelengths of <530 nm to reach the CIGS absorber. The (doped) ZnO layer, which is used in high-performance CIGS cells as the transparent conducting oxide material to collect the electrons from the cell, also contributes to the reduction in the loss in the photocurrent. Replacing ZnO with wider bandgap (Zn,Mg)O further increases the EQE[28]. For the present champion CIGS cell with a PCE of 22.9%, Cs was used in the alkali metal treatment[29]. The shape of the normalized EQE of the champion CIGS cell (area ≥1 cm^2) is now comparable to that of the c-Si cell. However, there remains a photocurrent loss in CIGS cells owing to the top transparent conductive oxide layer; this loss is common to all cells that use transparent conductive oxide windows. The V_{OC} and V_{MP} of the champion polycrystalline CIGS cell, which has a bandgap similar to that of c-Si, are now also comparable to those of c-Si (TABLE 1). Additional improvement in the V_{OC} and V_{MP} of CIGS cells could be achieved by further

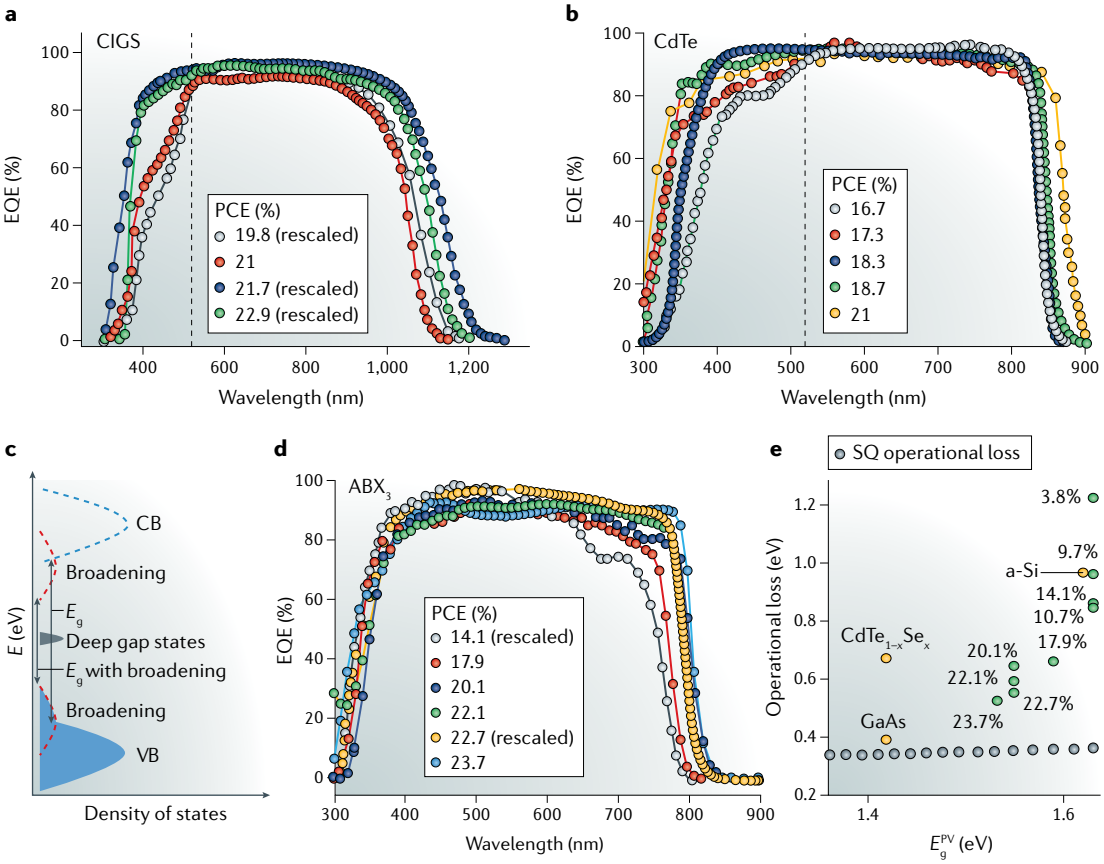

Fig. 5 | **Evolution of EQE in polycrystalline CIGS, CdTe and metal halide perovskite cells. a** | External quantum efficiency (EQE) values for the recent champion CIGS ($CuIn_xGa_{1-x}Se_2$) cells with different power conversion efficiencies (PCEs). **b** | EQE values for champion CdTe (or $CdTe_{1-x}Se_x$) cells. The dashed vertical lines indicate the bandgap (E_g) of CdS, a commonly used buffer layer in both CIGS and CdTe cells. **c** | Disorder-induced broadening of the E_g occurs in both CZTS (Cu_2ZnSnS_4) and CZTSS ($Cu_2ZnSnS_{4-y}Se_y$). **d** | Evolution of the EQE of small-area champion ABX_3 (where A is an organic cation, B is a metal cation and X is a halide) perovskite devices (with areas generally ≤0.2 cm^2). Normalized EQEs are rescaled (for the PCE = 19.8, 21.7 and 22.9% CIGS cells and the PCE = 14.1 and 22.7% ABX_3 cells) to match the reported short-circuit current densities of the cells. **e** | Evolution of the operational loss in small-area ABX_3 devices (green circles) as a function of the photovoltaic gap (E_g^{PV}). Data for the early cells with PCEs of 3.8%[75], 9.7%[76] and 10.7%[77] were not certified. For comparison, the operational losses of single-crystalline GaAs, amorphous Si (a-Si) and $CdTe_{1-x}Se_x$ (yellow circles) and the operational loss at open circuit in the Shockley–Queisser (SQ) limit (grey circles) are also shown. CB, conduction band; VB, valence band.

reducing interfacial recombination and by making the back surface highly reflective.

Polycrystalline CdTe. In the past 8 years, the PCE of polycrystalline CdTe-based solar cells has increased from 17.3% to 21%. Comparing the EQEs of the champion CdTe cells (FIG. 5b), we find a similar trend to that for CIGS cells, that is, the notable improvement in photocurrent efficiency for the higher-energy photons correlates with an increase in the PCE. In the champion CdTe cells, the losses due to the CdS layer, which is used to create the p–n junction with CdTe (Supplementary Fig. 8b), have been mostly eliminated, and the EQE seems to be limited only by the optical absorption of the glass–transparent conductive oxide substrate at short wavelengths.

The bandgap of a semiconductor can be tuned by changing the composition of the material. Although the change in bandgap is usually monotonic with the change in composition, in certain cases, there is a minimum bandgap at an intermediate composition of the two constituents with different bandgaps. This phenomenon is called bandgap 'bowing' and occurs in the $Cd(Te_{1-x}Se_x)$ and $Cd(Te_{1-x}S_x)$ alloys. On the basis of the known bandgap bowing effect in the $CdTe_{1-x}Se_x$ and $CdTe_{1-x}S_x$ systems and reports suggesting the use of $CdTe_{1-x}Se_x$ in First Solar modules[30], it is highly likely that the absorber material in the present champion device is not pure CdTe but $CdTe_{1-x}Se_x$ and/or $CdTe_{1-x}S_x$ (REF.[31]). The efficiency improvement can then be ascribed to bandgap grading in the polycrystalline CdTe absorber layer. Bandgap grading occurs when Se or S infiltrates the absorber material to produce $CdTe_{1-x}Se_x$ or $CdTe_{1-x}S_x$, respectively, which, for low Se or S contents, will extend optical absorbance to shorter wavelengths. As the champion cells are proprietary technologies, information about the processes used to reduce the detrimental effects of the CdS layer are not available in the public domain. However, academic studies suggest that a CdS:O layer may have been used to decrease the filtering effect and CdSe (which

can interdiffuse with the top of the CdTe layer to form $CdTe_{1-x}Se_x$) used together with the CdS layer to enable the use of a thinner CdS layer[32].

The J_{SC} of the champion CdTe cell is among the highest of any cell type, but V_{OC} losses remain. The V_{OC} in CdTe cells can be >1 V for single-crystalline CdTe-based cells combined with suitable interfacial materials[33]. In polycrystalline CdTe, minimization of non-radiative recombination at the grain boundaries and in the grain bulk (due to defects) will increase η_{int}, which, in turn, can reduce the operational loss of the cell. Indeed, cells based on polycrystalline CdTe have already shown V_{OC} values >900 mV (REF.[34]), an improvement that can be attributed to a reduction in non-radiative recombination.

Sustainable chalcogenides CZTSS and CZTS. The CIGS and CdTe cells discussed above each contain one or more elements that are relatively rare (for example, In, Ga and Te) in the Earth's crust. Moreover, In is in heavy demand for use in display technologies, solders and thermal interface materials[35]. The scarcity of the constituent materials makes large-scale production of CIGS and CdTe solar cells unsustainable. The rarer metals In and Ga can be substituted with less expensive, more earth-abundant and, in part, also more readily available elements (namely, Zn and Sn) to generate the more sustainable chalcogenide-based absorbers CZTS (Cu_2ZnSnS_4) and CZTSS ($Cu_2ZnSnS_{4-y}Se_y$). There has been substantial progress in solar cells based on CZTS and CZTSS thin films in the past 5 years, and the highest PCE of a sustainable chalcogenide-based cell is now 11.3%[10]. Owing to the similar ionic radii of Cu^+ and Zn^{2+} and the low formation energies for the neutral defect centres, the $[Cu_{Zn}^-, Zn_{Cu}^+]$ defect complex is prevalent in CZTSS and CZTS. The presence of these defects results in a significant density of states within the bandgap, an effect known as band tailing (FIG. 5c). Such tail states limit the possible light-induced separation between quasi-Fermi levels and, thus, limit the V_{OC}, as well as the current, and because of the increased probability of carrier recombination, they limit the PCE of the resulting cells[36]. The E_U in these systems can be ~50 meV (REFS[37,38]), which implies that even in the radiative limit, qV_{OC} is expected to be much lower than qV_{OC}^{SQ} because $J_0^{Rad} \gg J_0^{SQ}$.

The effects of alkali ion treatment of the absorber layer in CIGS have been highly beneficial, and similar developments may be possible for the CZTS and CZTSS systems. However, as pointed out early in the development of CIGS cells[39], such treatments are confined to the surface and cannot cancel the effects of bulk static disorder[40]. The bulk defect centres produced as a result of sulfur vacancies[41] have a large cross section for carrier trapping and subsequent non-radiative recombination and are hence known as killer defects. These killer defects lower the voltage output of a cell even when present in low concentrations. Indeed, eliminating killer defects[41] requires changes in the bulk of the materials, as they are a fundamental materials issue. As there is a considerable photocurrent loss due to the low EQE values at wavelengths of <530 nm in champion chalcogenide devices (Supplementary Fig. 9), it may be worth looking beyond the CdS–CZTS(S) interfaces to increase the photocurrent efficiencies for higher-energy photons. Moreover, owing to a cliff-like band offset at the CZTS–CdS interface, charge accumulation occurs. The charge accumulation leads to the non-radiative recombination of holes in the CZTS layer with the accumulated electrons in the CdS layer, which decreases η_{int} and results in the low V_{OC} of the CZTS cell. $Zn_{1-x}Cd_xS$ appears to be a better choice than CdS for the buffer layer, because $Zn_{1-x}Cd_xS$ has a wider bandgap and the band offset at the interface can be tuned by varying the Zn:Cd ratio. The effect of switching to $Zn_{1-x}Cd_xS$ is apparent from the increase in the EQE of CZTSS cells in the sub-520 nm region (Supplementary Fig. 9).

ABX_3 metal halide perovskites. Solar cells based on metal halide perovskites have shown more impressive progress in their PCE in the past 5 years than any other PV technology[42]. The similarity in preparation of polycrystalline thin films and post-preparation treatments of these materials to those used for organic electronics and/or dye-sensitized cells (for example, solution processing) on the one hand and other thin-film absorbers such as CIGS (for example, vapour-phase processing and interface modifications) on the other hand has helped to drive a huge research effort, which has undoubtedly contributed to the meteoric rise in the cell performances. The evolution of the EQE of certified small-area (<1 cm^2) champion cells is shown in FIG. 5d. The EQE is high for high-energy photons even in the early cells, unlike the case for the early CdTe and CIGS technologies. This high EQE is due, at least in part, to the use of a wide-bandgap, hole-transporting and electron-blocking selective contact (for example, 2,2′,7,7′-tetrakis(*N*,*N*-di-p-methoxyphenylamine)-9,9′-spirobifluorene) and an electron-transporting layer (typically, TiO_2) (Supplementary Fig. 8c) with good transmittance for high-energy photons. In addition, nearly all preparation methods yield materials with respectable diffusion lengths[43,44]. The increase in absolute photocurrents over the years is reflected in the improved EQE values near the band edge (FIG. 5d), which is the result of efficient photon absorption. Part of this 'optical' improvement is due to a shift from films with small crystalline domains (with a size of a few tens of nanometres) that are infiltrated into a porous scaffold to films with larger polycrystalline domains (with sizes ranging from hundreds of nanometres to micrometres). For the latter, the extinction coefficient near the band edge is greatly enhanced owing to reduced disorder in the excitonic absorption transition. The increased absorption in the red region of the electromagnetic spectrum can also be ascribed to the improved crystalline quality of the absorber (that is, to a decrease in trap-assisted recombination), which has enabled thicker films to operate well. The photocurrent has further increased owing to the use of slightly lower bandgap ABX_3 materials that result from having cation mixtures on the A site and specifically a transition to formamidinium-rich compositions, often with mixed halides on the X site.

Although high densities of native defects would be expected for materials that are prepared at low temperatures, there is no clear experimental evidence for this

for halide perovskites, which can be explained by defect healing[45] and/or defect tolerance[46,47]. The values of E_U, which are a measure of the presence, energy distribution and density of electronic states in the bandgap region, for polycrystalline ABX_3 approach those of GaAs and c-Si (REFS[48,49]). The evolution of the operational losses from past to present small-area champion cells (FIG. 5e) shows that the improvement in cell performance is concurrent with a decrease in operational loss. The contact materials appear to contribute significantly to the operational loss in perovskite cells (TABLE 1). It has been argued that the energy loss ($E_g^{PV} - qV_{OC}$) in ABX_3 perovskite cells could reach a value as low as that of GaAs, on the basis of η_{int} values of more than ~90% for ABX_3 films after molecular chemical surface passivation[50]. Although a high η_{int} is a necessary condition for reducing energy loss at open circuit, η_{ext} of the complete cell is what matters for the operational loss (of the complete cell). The need to maintain the achieved high η_{int} without (negatively) affecting the charge-transport properties across interfaces poses the challenge of making complete cells with optimized perovskite surfaces. One way to reduce interfacial recombination is to reduce the (interfacial) contact area between the charge recombination layer and the electrical contact layer.

Cells based on other materials

a-Si. Over the past decade, there has been almost no progress in the PV technology of a-Si, at least as far as the conversion efficiency is concerned. Presumably, this lack of progress is due, at least partly, to the intrinsic material limitations of the a-Si absorber (owing to its static disorder). This technology has the highest operational loss among all those we consider here. Approximately 35 years ago, it was shown that the presence of tail states in an amorphous semiconductor, such as a-Si, leads to several hundreds of millivolts of additional voltage loss in the system[51]. We argue that this intrinsic voltage loss (also observed in CZTSS and CZTS) is a bigger obstacle for market penetration than the much-studied initial intrinsic instability of the material, the so-called Staebler–Wronski effect. We do note, however, that a-Si is important for achieving high-efficiency c-Si SHJ cells, and although a-Si does not have the central role of absorber, the past developments in a-Si have enabled the present world-record c-Si efficiency, and thus, a-Si is a good example of cross-fertilization between PV technologies.

Quantum dot solar cells. In quantum dot (QD) cells, charge transport between the QDs is hindered because the surfaces of the QDs are often covered with higher-bandgap or insulating, typically organic, ligands. The presence of defects on QD surfaces also lowers the achievable photovoltage. Capping the surfaces of QDs with non-insulating materials is one approach to increasing the performance of cells made with them. For example, capping PbS QDs with $[PbX_3]^-$ and $[PbX]^+$ instead of the typical organic cations and anions reduces the tail states in the QDs[52], and solar cells with QDs capped with $[PbX_3]^-$ and $[PbX]^+$ show higher photovoltages than those with organic-ligand-capped QDs. Solar cells based on $CsPbI_3$ perovskite QDs capped with insulating long-alkyl-chain ligands have achieved PCEs of >10%[53]. Although the $CsPbI_3$ perovskite QDs in these cells were capped with insulating ligands, charge transport across the $CsPbI_3$ QDs was improved by adding[54] a small amount of formamidinium iodide to the $CsPbI_3$ QD arrays. The addition of formamidinium iodide decreased the interparticle distance between the QDs, leading to improved charge transport and yielding the impressive top PCE for this type of cell[54]. On the basis of this achievement, we envisage that there is now considerable room for further improvement in the photocurrent efficiency. It is debatable whether ABX_3 halide perovskites have simply engulfed the QD field (QDs have traditionally been based on III–V or metal chalcogenide semiconductors) or whether QDs remain a discrete technology.

Organic photovoltaics. Over the past decade, the PCE of certified (≥1 cm^2 in area) OPV champion single-junction devices has progressed from values of <10% to the current value of 11.2%. The present champion device (with an area of ~1 cm^2) uses a donor–acceptor-type polymer, [6,6]-phenyl-C_{71}-butyric acid methyl ester ($PC_{70}BM$), bulk heterojunction as the active layer[55]. The relatively poor voltage efficiency in an OPV device has origins in both charge separation and recombination. Part of the absorbed energy is used (and lost, in terms of photovoltage) to separate charges at the donor–acceptor interface and to form the charge-transfer states, which arise owing to the interaction between the donor and acceptor molecules. Although these charge-transfer states are photoactive, they generate negligible photocurrent. E_g^{PV} is mainly determined by the absorbance profile of the lower bandgap material, which can be either of the two materials that form the heterojunction. Charge-transfer states add more electronic states to those already present owing to the electronic disorder of the donor and acceptor materials. Both the absorption strength of charge-transfer states and their energy, E_{CT}, with respect to E_g^{PV} affect the voltage output of the cell. Thus, the key to improving the voltage efficiency is to minimize $|E_{CT} - E_g^{PV}|$ and to minimize photon absorption by charge-transfer states through the judicious design of materials, for example, by using non-fullerene acceptors[56].

Our analysis shows that the voltage efficiency of (≤1 cm^2 in area, non-certified) OPVs has indeed increased by minimizing $|E_{CT} - E_g^{PV}|$ (FIG. 6a,b and Supplementary Fig. 10). This improvement in voltage efficiency is mainly a result of a decrease in the loss factor, $kT\ln(J_0^{Rad}/J_0^{SQ})$, which is the fifth loss term in equation 5. A reduction in non-radiative recombination (the sixth and seventh terms in equation 5) has also contributed to the improved voltage efficiencies of OPVs. In an OPV device, non-radiative recombination at the donor–acceptor interface can be viewed as electron transfer in the Marcus inverted regime[57,58]. Within this regime, as the free energy of the process, given by E_{CT}, increases, the recombination rate decreases, which in turn increases the η_{ext} and results in higher voltage efficiency[58]. Energetic disorder at the interfaces and in the bulk, including structural disorder[40,59], also increases

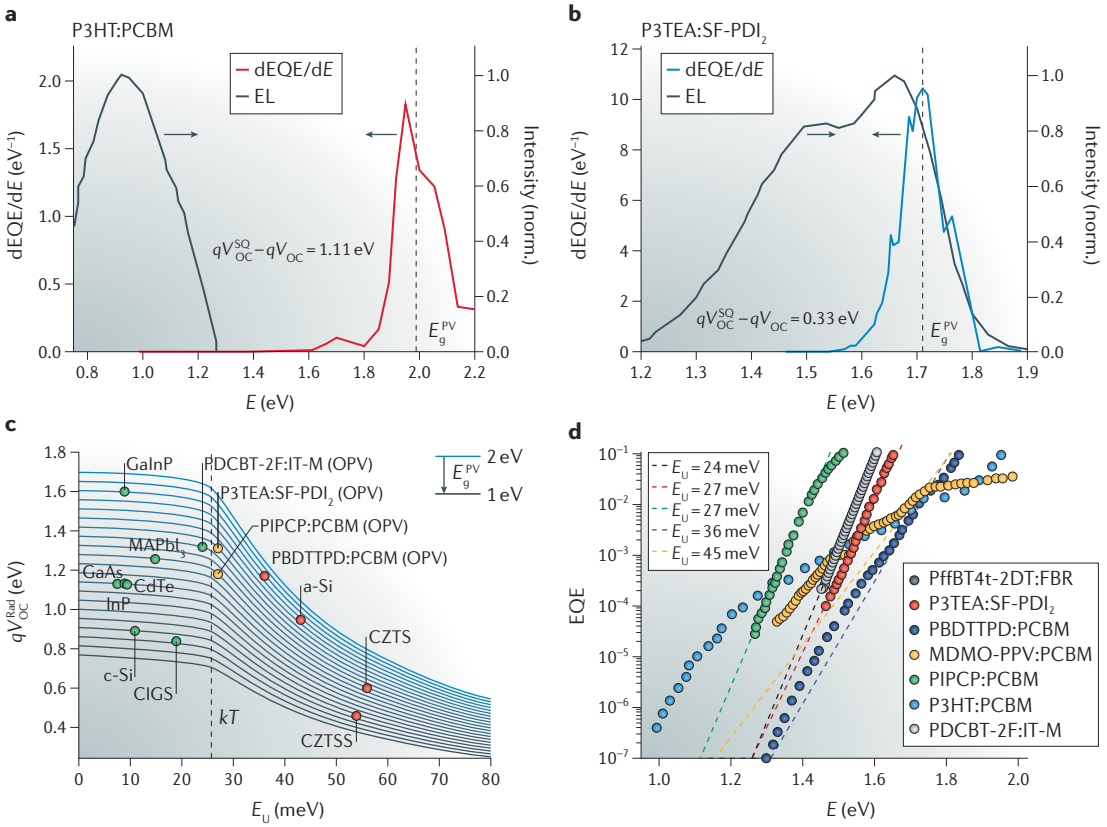

Fig. 6 | **Effects of sub-photovoltaic gap states. a,b** | Distribution of the bandgaps and electroluminescence (EL) spectra of P3HT:PCBM[78] (shown in panel **a**) and P3TEA:SF-PDI$_2$ (REF.[79]) (shown in panel **b**). The deviation from the Shockley–Queisser limit decreases as separation between the EL spectrum and the photovoltaic gap (E_g^{PV}) decreases (also see Supplementary Fig. 10). dEQE/dE is the probability distribution function of the distribution of Shockley–Queisser-type bandgap energies (where EQE is the external quantum efficiency and E is energy). **c** | Plot showing the values of qV_{OC}^{Rad} (where q is the elementary charge and V_{OC}^{Rad} is the open-circuit voltage in the radiative limit) versus the Urbach energy (E_U) for E_g^{PV} values in the range of 1–2 eV. The decrease in qV_{OC}^{Rad} is drastic when $E_U > kT$ (where k is the Boltzmann constant and T is the temperature, where $T = 298$ K). The expected qV_{OC}^{Rad} for different technologies based on their E_g^{PV} and typical E_U are shown (see Supplementary Table 4 for E_U values); green indicates no significant loss in voltage, yellow indicates that the material is not far from the optimal E_U value and red indicates significant voltage loss. **d** | EQE as a function of the excitation energy for different organic photovoltaics. The E_U associated with the different organic photovoltaics can be calculated from the plots (see Urbach energy determination in OPVs section in the Supplementary Information and Supplementary Fig. 11). Cells with an E_U close to kT show high voltage efficiency and an exponential decay of states. a-Si, amorphous Si; CIGS, $CuIn_xGa_{1-x}Se_2$; c-Si, single-crystalline Si; CZTS, Cu_2ZnSnS_4; CZTSS, $Cu_2ZnSnS_{4-y}Se_y$; MA^+, methylammonium; mc-Si, multicrystalline Si; OPV, organic photovoltaic; QD, quantum dot.

the probability of non-radiative recombination. In an organic blend, energy back transfer from the charge-transfer state to the donor material can occur, which enables electron–hole recombination to proceed via the electronic states of the pristine organic material[60]. In this scenario, if the donor material has a high PLQY, then non-radiative recombination can be further supressed. However, note that the inherent presence of high-energy vibrational modes (especially in the C=C bonds that are omnipresent in organic conductors) can lead to a loss of ~160 meV owing to non-radiative recombination[58,61].

Tail states and voltage efficiency

There is an exponential decrease in the density of electronic states from the band edges in semiconductors. Here, we discuss to what extent these tail states influence the voltage output. We limit our discussion to the voltage, because in real devices, the tail states produce negligible current (and have very little influence on the value of E_g^{PV}). Starting from an earlier reported approach[62], we estimate the impact of E_U on the achievable photovoltage for materials with different values of E_g^{PV}. In FIG. 6c, we plot our estimates of qV_{OC}^{Rad} for different values of E_g^{PV} (between 1 eV and 2 eV) as a function of E_U (see Methods section in Supplementary Information). The decrease in the value of qV_{OC}^{Rad} is small for $E_U < kT$ (for example, qV_{OC}^{Rad} decreases by 10 meV for E_U = 15 meV) but increases rapidly once the value of E_U exceeds kT (~26 meV at $T \approx 298$ K).

Single-crystalline GaAs, Si, GaInP and InP, and polycrystalline CdTe, ABX_3 and CIGS, all have E_U values below kT (FIG. 6c and Supplementary Table 4). The simplified equation 7 can therefore be used for estimating the V_{OC} or radiative efficiencies for these technologies with good accuracy. For technologies such as a-Si, CZTS

and CZTSS, the E_U values are >40 meV, leading to an additional loss of several hundred meV in the radiative limit. The band tailing in CZTS and CZTSS originates from the static disorder that is inherent to these materials; even in their single crystals, $E_U >> kT$ (REF.[37]). A high E_U severely limits the voltage efficiency of cells using that material as the absorber, as is the case for a-Si. Thus, unless it is shown that a high E_U is not inherent to CZTS and CZTSS, the PCE of cells that use these materials as absorbers will be limited.

In OPV cells, the EQE below E_g^{PV} has a contribution from the charge-transfer states as well as from energetic disorder, which is inherent to the pristine materials (see FIG. 6d and 'Urbach energy determination in OPVs' section in the Supplementary Information). In the cells with a higher voltage efficiency, we do not see any notable photocurrent due to the charge-transfer absorbance states, which indicates that either the oscillator strength of the charge-transfer states is very weak or that their energies are so close to E_g^{PV} that we cannot distinguish absorbance due to such states. E_U values are ~40–50 meV for cells with a low voltage efficiency but are close to or less than 26 meV (that is, kT at 298 K) for those with a high voltage efficiency. Thus, a-Si-like (static) disorder in OPVs, which is reflected in a high E_U value, is no longer a factor in the voltage loss, as E_U is now less than kT (REFS[60,63]) (FIG. 6d).

Scale-up limit

Although the fundamental physics and chemistry of a particular solar cell do not change while scaling up the size of a cell, maintaining the electronic quality over large areas and achieving the high manufacturing yields necessary to be able to build modules are challenging and require the ability to reproducibly fabricate large-area cells. Scaling up PVs requires a progression from small-area (<<1 cm²) cells to 1 cm² (or larger) cells to mini-modules (areas of <500 cm²) to large-area modules (≥800 cm²) and, finally, to commercial large-area modules. The progress, in terms of PCE, in scaling up the different PV technologies is shown in FIG. 7a. Typically, the FF is the first bottleneck during scale up from small-area to large-area PV cells. FIGURE 7b shows how the FF values differ between small-area and large-area cells. The simulated FF values are calculated using the following relation:

$$\mathrm{FF} = \frac{V'_{OC} - \ln(V'_{OC} - \ln(V'_{OC}+1)+1)}{V'_{OC}} \times \frac{V'_{OC} - \ln(V'_{OC}+1)}{V'_{OC} - \ln(V'_{OC}+1)+1} \quad (9)$$

(see the section Relationship between the fill factor and V_{OC} in the Supplementary Information for the derivation and REF.[64] for an empirical formula).

The transition from small-area to 1 cm² cells should be quick once control over material and interface quality for an area of 1 cm² is achieved; after this, scale up often becomes harder. There is room for significant future progress in, particularly, halide perovskite technologies by increasing the FF of these cells. For CdTe and OPVs, the FFs for large-area and small-area cells are already quite similar.

c-Si and mc-Si technologies show the best scale-up performance of PV cells, which is to be expected following more than 60 years of development. For each type of c-Si cell architecture, there is an ~3–4% drop in efficiency from the champion laboratory cell to the commercial modules. The GaAs-based modules (certified) have comparable efficiencies to those of c-Si (which have an area that is 15 times larger), although the former

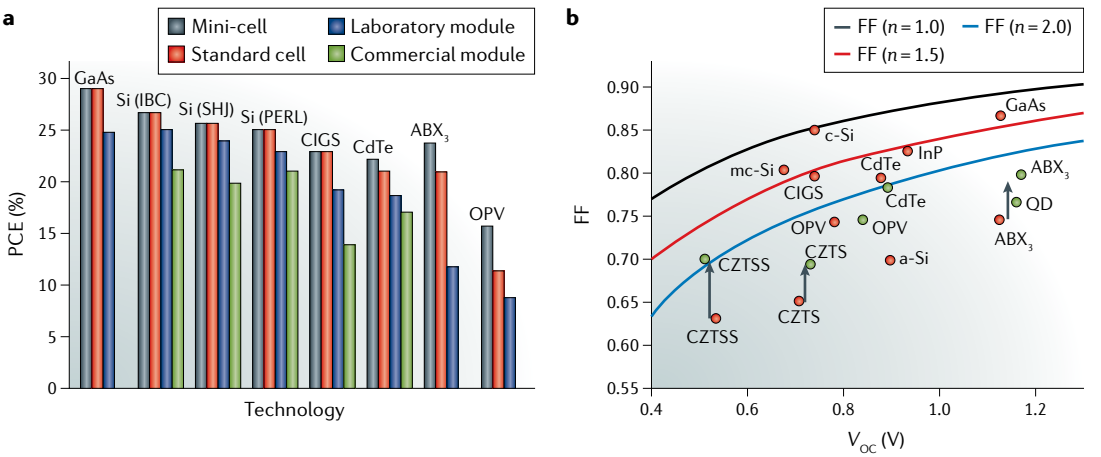

Fig. 7 | **Progress in the scale up of solar cells. a** | The power conversion efficiencies (PCEs) of mini-cells (area of <1 cm²), standard cells (area of ≥1 cm²) and modules (≥800 cm²) for various photovoltaic technologies. **b** | The fill factor (FF) for champion cells of the different photovoltaic technologies. Values are for mini-cells (green circles; data from REF.[80] (CZTSS), REF.[74] (CZTS), REF.[20] (OPV) and REF.[81] (ABX_3)) and standard cells (red circles; data in TABLE 1 and Supplementary Table 2). FF values have also been calculated using equation 9 as a function of the open-circuit voltage (V_{OC}) for different values of the diode ideality factor (n, which can be extracted from the dark current–voltage curve). ABX_3, metal halide perovskite; a-Si, amorphous Si; CIGS, $CuIn_xGa_{1-x}Se_2$; c-Si, single-crystalline Si; CZTS, Cu_2ZnSnS_4; CZTSS, $Cu_2ZnSnS_{4-y}Se_y$; IBC, interdigitated back contact; mc-Si, multicrystalline Si; OPV, organic photovoltaic; PERL, passivated emitter and rear locally diffused; SHJ, Si heterojunction; QD, quantum dot.

has a higher single-cell efficiency. There have been substantial improvements in both module and laboratory cell efficiencies in CIGS and CdTe technologies in the past 5 years, as well in OPV and emerging halide-perovskite-based technologies. For halide perovskites, progress from laboratory cells to modules is still far behind that of Si; this is probably a result of the unprecedented development of single cells (mainly in academia), as we do not know of any fundamental obstacles.

As there is always a time lag for the transition from laboratory to commercial module fabrication and optimization, we expect that all the non-Si technologies will follow the development pattern of c-Si but with delay owing to less intensive optimization efforts. Because polycrystalline CdTe (or Cd(Te,Se)) technologies are commercial, they should follow mc-Si PV development particularly closely in the next few years.

Outlook

Although we have mainly discussed the scientific and technological efforts behind the evolution of the different solar cell technologies, economic cost factors, as well as local political will and global politics, have had a pivotal role in the development of particular technologies and will continue to do so in the future. Increasing public awareness of the need for sustainable and clean energy sources has certainly helped and supports ongoing R&D of solar cell technologies.

For the established solar cell technologies, for which commercial modules are available (for example, c-Si, CIGS and CdTe), all development of the champion cells has been carried out by commercial companies rather than in academic laboratories. We can expect the same to happen with those cell technologies that are near commercialization but for which present cell development is dominated by academia.

The developments in the single-crystalline-based devices and polycrystalline CIGS and CdTe devices have occurred mostly through modification of the interfaces and/or changes in device architecture, which indicates that the development of the absorber materials in these cases is reaching a plateau. A major development in the two commercial polycrystalline technologies is that the CdS buffer layer has either been eliminated or alloyed, such that its presence no longer has a detrimental effect on the current. Focused research on the interfaces to eliminate recombination and other losses that originate at interfaces and optimization of the device architecture will further improve cell performances. To this end, cross-fertilization between established and emerging technologies, as has been seen for GaAs and GaInP, as well as CIGS and CdTe technologies, can be very fruitful.

The progress in the development of c-Si technologies has seen its PCE come close to the maximum possible PCE of 29.4%[22]. We expect that the c-Si cell technology with the SHJ–IBC architecture, which is a scalable technology, will reinforce the position of c-Si as the market leader in the single-junction cell category. At present, a cell with an area of 79 cm^2 has already demonstrated a PCE of 26.7%, and a cell with an area of 180 cm^2 (which would be a truly amazing size for other PV technologies) reached a PCE of 26.6%. These cell results lead us to anticipate that the module efficiency will also increase in the near future. However, we expect only minor progress in mc-Si technology, as the SHJ–IBC technology used in the champion c-Si cell may not be suitable for mc-Si owing to the intrinsically lower carrier diffusion lengths in mc-Si than in c-Si.

GaAs technology has almost reached its voltage limit, although a small improvement in the photocurrent efficiency is expected. GaInP cells are mostly small (<1 cm^2) in area because they are used in concentrator cells. Possibly, future work on larger-area GaInP cells will be able to determine whether the contacts have a drastic effect on the operational loss. The performance of InP cell technology can catch up with that of GaAs and GaInP cells owing to the similar electronic quality of the absorber and interfacial materials used in these technologies.

In halide perovskite technologies, there is a need to decrease the operational loss for the standard 1 cm^2 cells. Although overshadowed by the achievements of very small laboratory cells, the improvements in stabilities and in increasing cell area are as impressive and should pave the way to modules with higher PCEs. In this assessment, we have focused only on the fundamental properties of single-junction PV cells. However, metal halide perovskites are highly suited for multijunction approaches owing to their compositionally tuneable bandgap. A multijunction approach has already led to a 1 cm^2 perovskite-on-Si tandem cell with a certified PCE of 28%[65], and thus, this is likely to be a technologically relevant approach. However, the commercial viability of this technology will depend on the long-term stability under realistic conditions.

Further R&D in a-Si technology will likely be discouraged owing to the rapid progress of alternative thin-film technologies based on CdTe and CIGS and the emergence of halide perovskites as PV materials, all of which are higher quality optoelectronic materials than a-Si. Thus, it would seem that significant development of the materials and/or device structure or identification of a unique market will be needed for progress in a-Si technology.

Although the certified record efficiency for a single-junction OPV cell with an area of ≥1 cm^2 remains at 11.2%, a small-area (0.04 cm^2) cell has been reported with a PCE of 15.6%, indicating rapid progress in the OPV technology[10]. However, cells that include the innovations that yield E_U values below or around the critical kT threshold, which lead to high voltage efficiency, are yet to be certified. The $E_g^{PV} - E_{CT}$ value and the value of E_U appear to be correlated. If there is a connection between them, many other donor–acceptor combinations can be designed for OPVs. On the basis of the recent progress in the development of OPV materials, we expect rapid improvements in the record efficiencies for OPVs over the next few years. By contrast, the prevalence of electronic defects in CZTS and CZTSS, which appears to be inherent in these materials, will limit their development and may make them obsolete.

The earth abundance and the availability (which are not the same) of elements (that is, of the mineable minerals that contain them) required for the various

PV technologies differ significantly. If we limit ourselves to the PV absorber materials, then it is hard to beat Si technologies, which are based on the second most abundant element in the Earth's crust. To compare the relative abundance of elements, we use 10^6 atoms of Si as a point of reference for abundance, as suggested previously[66]. The abundance of Cu, Zn, Sn and Pb (used in various polycrystalline solar cells) is around 10–100 atoms per 10^6 Si atoms. If we set an arbitrary limit of 0.1 atoms per 10^6 Si atoms as the threshold for sustainability, In, Se, Cd and I are just above the limit, whereas Te is significantly below the limit.

Concerning environmental issues of PV technologies, it is clear that appropriate considerations and deployment strategies must be investigated and adopted. Two of the elements that raise ecotoxicity concerns are Cd, used in commercial CdTe technologies, and Pb, used in emerging thin-film metal halide perovskite PV cells. Extensive work with CdTe over the past 15 years (primarily driven by First Solar) has established safe methods for manufacturing, deploying and recycling CdTe PV modules[67]. The very low solubility product of CdTe in water also minimizes the danger of groundwater contamination by Cd.

Pb-based halide perovskite PV technology is much younger than the others considered here. However, initial life cycle analysis has revealed that the toxicological impact of Pb is likely to be less than 0.3% of the total ecotoxicity impact of manufacturing and deploying Pb-based halide-perovskite-on-Si PV modules, even with the unrealistic boundary condition that all the Pb is eventually leached into the environment[68]. However, to fully establish the safety of the manufacturing, use and end-of-life disposal of metal halide perovskite PV modules, a large and substantiated body of evidence is required to understand the full life cycle.

For OPVs and, to some extent, for the metal halide perovskites (and other organic materials used in the cells), the environmental effects of solvents used in the preparation also need to be considered. For a more balanced and complete view of the environmental impact of a PV technology, we note that commonly used materials, such as In, in indium tin oxides and even Si in Si PV cells also have an environmental impact, which is largely a result of the energy cost of mining and/or purifying these materials.

On the basis of today's market and predicted future markets, PV technologies will become an alternative for c-Si and mc-Si, or complementary to them, only if production yields and the stabilities of these alternative technologies are comparable to those of the Si technologies. A likely near-term future technology is affordable Si tandem cells, which may well become commercial within a few years. Commercialization of Si tandem cells will require the fabrication of a wider bandgap cell on top of a Si cell to overcome the SQ single-junction efficiency limit, with comparable lifetime and minimal added cost. The champion certified tandem cells, based on GaAs-on-Si, have areas of <5 cm^2, with most around 1 cm^2. Because the future of c-Si modules will be based on large-area cells, metal-halide-perovskite-based cells appear key contenders for top cells for tandem cell applications. In addition, recent improvements in (decreasing) operational losses for OPV cells and impressive improvements in OPV tandem cells[69] have made OPVs a possible option for viable top cells.

As the past 5 years that we have focused on here illustrate, there are often surprising developments in PVs, partly because of unexpected results that researchers stumble on and, with a prepared mind, recognize as being valuable, partly because of brilliant empirical optimization and partly because basic research into 'strange' results leads to new or better fundamental scientific insights. Industrial development needs both the first and the last, because experience teaches that without these, new directions are rarely identified, and empirical optimization has its limits. Thus, it is worthwhile from time to time to stop, look around and take stock of where we are, so as to give ideas of where and how to move forward, which is a major goal of this analysis.

Published online 28 March 2019

1. Shockley, W. & Queisser, H. J. Detailed balance limit of efficiency of *p–n* junction solar cells. *J. Appl. Phys.* **32**, 510–519 (1961).
2. Nayak, P. K., Bisquert, J. & Cahen, D. Assessing possibilities and limits for solar cells. *Adv. Mater.* **23**, 2870–2876 (2011).
This study introduces operational loss as a parameter for the comparison and analysis of solar cell technologies.
3. Nayak, P. K. & Cahen, D. Updated assessment of possibilities and limits for solar cells. *Adv. Mater.* **26**, 1622–1628 (2014).
4. Rau, U., Blank, B., Müller, T. C. M. & Kirchartz, T. Efficiency potential of photovoltaic materials and devices unveiled by detailed-balance analysis. *Phys. Rev. Appl.* **7**, 044016 (2017).
This study introduces the concept of determining the photovoltaic gap of a solar cell from the EQE of the cell.
5. Wang, Y. et al. Optical gaps of organic solar cells as a reference for comparing voltage losses. *Adv. Energy Mater.* **8**, 1801352 (2018).
6. Markvart, T. The thermodynamics of optical étendue. *J. Opt. A* **10**, 015008 (2008).
7. Hirst, L. C. & Ekins-Daukes, N. J. Fundamental losses in solar cells. *Prog. Photovolt.* **19**, 286–293 (2011).
This article provides analytical expressions for the fundamental losses in solar cells.
8. Miller, O. D., Yablonovitch, E. & Kurtz, S. R. Strong internal and external luminescence as solar cells approach the Shockley–Queisser limit. *IEEE J. Photovolt.* **2**, 303–311 (2012).
9. Rau, U. Reciprocity relation between photovoltaic quantum efficiency and electroluminescent emission of solar cells. *Phys. Rev. B* **76**, 085303 (2007).
10. Green, M. A. et al. Solar cell efficiency tables (version 53). *Prog. Photovolt.* **27**, 3–12 (2019).
This article provides solar cell parameters for the state-of-the-art cells.
11. Schnitzer, I., Yablonovitch, E., Caneau, C. & Gmitter, T. J. Ultrahigh spontaneous emission quantum efficiency, 99.7% internally and 72% externally, from AlGaAs/GaAs/AlGaAs double heterostructures. *Appl. Phys. Lett.* **62**, 131–133 (1993).
12. Green, M. A. Radiative efficiency of state-of-the-art photovoltaic cells. *Prog. Photovolt.* **20**, 472–476 (2012).
13. Sheng, X. et al. Device architectures for enhanced photon recycling in thin-film multijunction solar cells. *Adv. Energy Mater.* **5**, 1400919 (2015).
14. Geisz, J. F., Steiner, M. A., García, I., Kurtz, S. R. & Friedman, D. J. Enhanced external radiative efficiency for 20.8% efficient single-junction GaInP solar cells. *Appl. Phys. Lett.* **103**, 041118 (2013).
15. Steiner, M. A. et al. CuPt ordering in high bandgap $Ga_xIn_{1-x}P$ alloys on relaxed GaAsP step grades. *J. Appl. Phys.* **106**, 063525 (2009).
16. Green, M. A. et al. Solar cell efficiency tables (version 49). *Prog. Photovolt.* **25**, 3–13 (2017).
17. Wanlass, M. Systems and methods for advanced ultra-high-performance InP solar cells. US Patent US9590131B2 (2014).
18. Green, M. A., Emery, K., Hishikawa, Y., Warta, W. & Dunlop, E. D. Solar cell efficiency tables (version 42). *Prog. Photovolt.* **21**, 827–837 (2013).
19. Yoshikawa, K. et al. Silicon heterojunction solar cell with interdigitated back contacts for a photoconversion efficiency over 26%. *Nat. Energy* **2**, 17032 (2017).
This study presents an efficient (PCE = 26.6%) c-Si solar cell with the IBC–SHJ architecture.
20. Green, M. A. et al. Solar cell efficiency tables (version 52). *Prog. Photovolt.* **26**, 427–436 (2018).
21. Taguchi, M. et al. 24.7% record efficiency HIT solar cell on thin silicon wafer. *IEEE J. Photovolt.* **4**, 96–99 (2014).
22. Richter, A., Hermle, M. & Glunz, S. W. Reassessment of the limiting efficiency for crystalline silicon solar cells. *IEEE J. Photovolt.* **3**, 1184–1191 (2013).
23. Trupke, T., Zhao, J., Wang, A., Corkish, R. & Green, M. A. Very efficient light emission from bulk crystalline silicon. *Appl. Phys. Lett.* **82**, 2996–44107 (2003).

24. Yang, Y. M. et al. Development of high-performance multicrystalline silicon for photovoltaic industry. *Prog. Photovolt.* **23**, 340–351 (2015).
25. Macdonald, D. & Geerligs, L. J. Recombination activity of interstitial iron and other transition metal point defects in p- and n-type crystalline silicon. *Appl. Phys. Lett.* **85**, 4061–4063 (2004).
26. Benick, J. et al. High-efficiency n-type HP mc silicon solar cells. *IEEE J. Photovolt.* **7**, 1171–1175 (2017).
27. Chirilă, A. et al. Potassium-induced surface modification of Cu(In,Ga)Se_2 thin films for high-efficiency solar cells. *Nat. Mater.* **12**, 1107–1111 (2013).
28. Chantana, J., Kato, T., Sugimoto, H. & Minemoto, T. Thin-film Cu(In,Ga)$(Se,S)_2$-based solar cell with (Cd,Zn)S buffer layer and $Zn_{1-x}Mg_xO$ window layer. *Prog. Photovolt.* **25**, 431–440 (2017).
29. Kato, T., Wu, J.-L., Hirai, Y., Sugimoto, H. & Bermudez, V. Record efficiency for thin-film polycrystalline solar cells up to 22.9% achieved by Cs-treated Cu(In,Ga)$(Se,S)_2$. *IEEE J. Photovolt.* **9**, 325–330 (2018).
30. IEEE Electron Devices Society. IEEE Electron Devices Society Newsletter: highlights of the 2017 IEEE Photovoltaic Specialists Conference. *IEEE* https://eds.ieee.org/images/files/newsletters/newsletter_oct17.pdf (2017).
31. Poplawsky, J. D. et al. Structural and compositional dependence of the $CdTe_xSe_{1-x}$ alloy layer photoactivity in CdTe-based solar cells. *Nat. Commun.* **7**, 12537 (2016).
32. Paudel, N. R., Poplawsky, J. D., Moore, K. L. & Yan, Y. Current enhancement of CdTe-based solar cells. *IEEE J. Photovolt.* **5**, 1492–1496 (2015).
33. Zhao, Y. et al. Monocrystalline CdTe solar cells with open-circuit voltage over 1 V and efficiency of 17%. *Nat. Energy* **1**, 16067 (2016).
34. Gloeckler, M., Sankin, I. & Zhao, Z. CdTe solar cells at the threshold to 20% efficiency. *IEEE J. Photovolt.* **3**, 1389–1393 (2013).
35. Lokanc, M., Eggert, R. & Redlinger, M. The availability of indium: the present, medium term, and long term. *NREL* https://www.nrel.gov/docs/fy16osti/62409.pdf (2015).
36. Gokmen, T., Gunawan, O., Todorov, T. K. & Mitzi, D. B. Band tailing and efficiency limitation in kesterite solar cells. *Appl. Phys. Lett.* **103**, 103506 (2013).
37. Ng, T. M. et al. Optoelectronic and spectroscopic characterization of vapour-transport grown Cu_2ZnSnS_4 single crystals. *J. Mater. Chem. A* **5**, 1192–1200 (2017).
38. Yan, C. et al. Beyond 11% efficient sulfide kesterite $Cu_2Zn_xCd_{1-x}SnS_4$ solar cell: effects of cadmium alloying. *ACS Energy Lett.* **2**, 930–936 (2017).
39. Kronik, L., Cahen, D. & Schock, H. W. Effects of sodium on polycrystalline Cu(In, Ga)Se_2 and its solar cell performance. *Adv. Mater.* **10**, 31–36 (1998).
40. Nayak, P. K., Garcia-Belmonte, G., Kahn, A., Bisquert, J. & Cahen, D. Photovoltaic efficiency limits and material disorder. *Energy Environ. Sci.* **5**, 6022 (2012).
41. Kim, S., Park, J. S. & Walsh, A. Identification of killer defects in kesterite thin-film solar cells. *ACS Energy Lett.* **3**, 496–500 (2018).
42. Snaith, H. J. Present status and future prospects of perovskite photovoltaics. *Nat. Mater.* **17**, 372–376 (2018).
This is a recent review on halide perovskite materials for optoelectronic applications.
43. Stranks, S. D. et al. Electron-hole diffusion lengths exceeding 1 micrometer in an organometal trihalide perovskite absorber. *Science* **342**, 341–344 (2013).
44. Edri, E. et al. Elucidating the charge carrier separation and working mechanism of $CH_3NH_3PbI_{3-x}Cl_x$ perovskite solar cells. *Nat. Commun.* **5**, 3461 (2014).
45. Ceratti, D. R. et al. Self-healing inside $APbBr_3$ halide perovskite crystals. *Adv. Mater.* **30**, 1706273 (2018).
46. Brandt, R. E., Stevanovic, V., Ginley, D. S. & Buonassisi, T. Identifying defect-tolerant semiconductors with high minority-carrier lifetimes: beyond hybrid lead halide perovskites. *MRS Commun.* **5**, 265–275 (2015).
47. Zakutayev, A. et al. Defect tolerant semiconductors for solar energy conversion. *J. Phys. Chem. Lett.* **5**, 1117–1125 (2014).
48. De Wolf, S. et al. Organometallic halide perovskites: sharp optical absorption edge and its relation to photovoltaic performance. *J. Phys. Chem. Lett.* **5**, 1035–1039 (2014).
49. Sutter-Fella, C. M. et al. Band tailing and deep defect states in $CH_3NH_3Pb(I_{1-x}Br_x)_3$ perovskites as revealed by sub-bandgap photocurrent. *ACS Energy Lett.* **2**, 709–715 (2017).
50. Braly, I. L. et al. Hybrid perovskite films approaching the radiative limit with over 90% photoluminescence quantum efficiency. *Nat. Photonics* **12**, 355–361 (2018).
51. Tiedje, T. Band tail recombination limit to the output voltage of amorphous silicon solar cells. *Appl. Phys. Lett.* **40**, 627–629 (1982).
This article demonstrates the effect of tail states on the efficiency of solar cells.
52. Liu, M. et al. Hybrid organic–inorganic inks flatten the energy landscape in colloidal quantum dot solids. *Nat. Mater.* **16**, 258–263 (2017).
53. Swarnkar, A. et al. Quantum dot-induced phase stabilization of α-$CsPbI_3$ perovskite for high-efficiency photovoltaics. *Science* **354**, 92–95 (2016).
54. Sanehira, E. M. et al. Enhanced mobility $CsPbI_3$ quantum dot arrays for record-efficiency, high-voltage photovoltaic cells. *Sci. Adv.* **3**, eaao4204 (2017).
55. Mori, S. et al. Organic photovoltaic module development with inverted device structure. *Mater. Res. Soc. Symp. Proc.* **1737**, 26–31 (2015).
56. Yan, C. et al. Non-fullerene acceptors for organic solar cells. *Nat. Rev. Mater.* **3**, 18003 (2018).
57. Marcus, R. A. Electron transfer reactions in chemistry. Theory and experiment. *Rev. Mod. Phys.* **65**, 599–610 (1993).
58. Benduhn, J. et al. Intrinsic non-radiative voltage losses in fullerene-based organic solar cells. *Nat. Energy* **2**, 17053 (2017).
59. Nayak, P. K. et al. The effect of structural order on solar cell parameters, as illustrated in a SiC-organic junction model. *Energy Environ. Sci.* **6**, 3272 (2013).
60. Qian, D. et al. Design rules for minimizing voltage losses in high-efficiency organic solar cells. *Nat. Mater.* **17**, 703–709 (2018).
61. Chen, X. K. & Brédas, J. L. Voltage losses in organic solar cells: understanding the contributions of intramolecular vibrations to nonradiative recombinations. *Adv. Energy Mater.* **8**, 1702227 (2018).
62. Jean, J. et al. Radiative efficiency limit with band tailing exceeds 30% for quantum dot solar cells. *ACS Energy Lett.* **2**, 2616–2624 (2017).
63. Venkateshvaran, D. et al. Approaching disorder-free transport in high-mobility conjugated polymers. *Nature* **515**, 384–388 (2014).
64. Green, M. A. Accuracy of analytical expressions for solar cell fill factors. *Solar Cells* **7**, 337–340 (1982).
65. Oxford PV. Oxford PV perovskite solar cell achieves 28% efficiency. *Oxford PV* https://www.oxfordpv.com/news/oxford-pv-perovskite-solar-cell-achieves-28-efficiency (2018).
66. Haxel, G. B., Hedrick, J. B. & Orris, G. J. Rare earth elements: critical resources for high technology: US Geological Survey fact sheet 087–02. *USGS* https://pubs.usgs.gov/fs/2002/fs087-02/ (updated 17 May 2005).
67. Chuangchote, S. et al. Review of environmental, health and safety of CdTe photovoltaic installations throughout their life-cycle. *First Solar* http://www.firstsolar.com/-/media/First-Solar/Sustainability-Documents/Sustainability-Peer-Reviews/Thai-EHS-Peer-Review_EN.ashx (2012).
68. CHEOPS. First results regarding the environmental impact of perovskite/silicon tandem PV modules. *CHEOPS* https://www.cheops-project.eu/news-in-brief/first-results-regarding-the-environmental-impact-of-perovskitesilicon-tandem-pv-modules (2017).
69. Meng, L. et al. Organic and solution-processed tandem solar cells with 17.3% efficiency. *Science* **361**, eaat2612 (2018).
70. Ekins-Daukes, N. J. & Hirst, L. C. in *24th European Photovoltaic Solar Energy Conf.* 457–461 (WIP-Munich, 2009).
71. Green, M. A., Emery, K., Hishikawa, Y., Warta, W. & Dunlop, E. D. Solar cell efficiency tables (version 40). *Prog. Photovolt.* **20**, 606–614 (2012).
72. Green, M. A., Emery, K., Hishikawa, Y., Warta, W. & Dunlop, E. D. Solar cell efficiency tables (version 47). *Prog. Photovolt.* **24**, 3–11 (2016).
73. Adachi, D., Hernández, J. L. & Yamamoto, K. Impact of carrier recombination on fill factor for large area heterojunction crystalline silicon solar cell with 25.1% efficiency. *Appl. Phys. Lett.* **107**, 233506 (2015).
74. Green, M. A. et al. Solar cell efficiency tables (version 50). *Prog. Photovolt.* **25**, 668–676 (2017).
75. Kojima, A., Teshima, K., Shirai, Y. & Miyasaka, T. Organometal halide perovskites as visible-light sensitizers for photovoltaic cells. *J. Am. Chem. Soc.* **131**, 6050–6051 (2009).
76. Kim, H.-S. et al. Lead iodide perovskite sensitized all-solid-state submicron thin film mesoscopic solar cell with efficiency exceeding 9%. *Sci. Rep.* **2**, 591 (2012).
77. Lee, M. M., Teuscher, J., Miyasaka, T., Murakami, T. N. & Snaith, H. J. Efficient hybrid solar cells based on meso-superstructured organometal halide perovskites. *Science* **338**, 643–647 (2012).
78. Gong, W. et al. Influence of energetic disorder on electroluminescence emission in polymer: fullerene solar cells. *Phys. Rev. B* **86**, 024201 (2012).
79. Liu, J. et al. Fast charge separation in a non-fullerene organic solar cell with a small driving force. *Nat. Energy* **1**, 16089 (2016).
80. Green, M. A., Emery, K., Hishikawa, Y., Warta, W. & Dunlop, E. D. Solar cell efficiency tables (version 44). *Prog. Photovolt.* **22**, 701–710 (2014).
81. Green, M. A. et al. Solar cell efficiency tables (version 51). *Prog. Photovolt.* **26**, 3–12 (2018).
82. Green, M. A., Emery, K., Hishikawa, Y., Warta, W. & Dunlop, E. D. Solar cell efficiency tables (Version 45). *Prog. Photovolt.* **23**, 1–9 (2015).

Acknowledgements
The authors acknowledge the support from the UK Engineering and Physical Sciences Research Council (grant nos EP/P032591/1 and EP/M015254/2) and thank B. Wenger, T. Markvardt, T. Kirchartz, T. Buonassisi and A. Bakulin for critical comments and data and D. Friedman for providing a GaAs cell. D.C. thanks the Weizmann Institute of Science, where he held the Rowland and Sylvia Schaefer Chair in Energy Research, for partial support.

Author contributions
All authors contributed to the discussion of content. P.K.N. researched most of the data, carried out the analysis and wrote the article. D.C. and S.M. contributed to the research-ing of data and analysis. D.C., H.J.S. and P.K.N. edited the manuscript before submission.

Competing interests
H.J.S. is the co-founder and CSO of Oxford PV Ltd, a company that is commercializing perovskite photovoltaic technologies. P.K.N., S.M. and D.C. declare no competing interests.

Publisher's note
Springer Nature remains neutral with regard to jurisdictional claims in published maps and institutional affiliations.

Supplementary information
Supplementary information is available for this paper at https://doi.org/10.1038/s41578-019-0097-0.

RELATED LINKS
Reference Solar Spectral Irradiance: Air Mass 1.5:
https://rredc.nrel.gov/solar//spectra/am1.5/#about